



Full length article

An energetically consistent two-scale asymptotic approach for modeling dynamic deformation and fracture of brittle materials

Quanzhang Li^{a,b}, Yipeng Rao^c, Xia Tian^d, Jun Chen^a, Xin Yu^a, Junzhi Cui^b, Meizhen Xiang^{a,*}^a National Key Laboratory of Computational Physics, Institute of Applied Physics and Computational Mathematics, Beijing, 100088, China^b LSEC, ICMSEC, Academy of Mathematics and Systems Sciences, CAS, Beijing, 100090, China^c Institute for Computing and Digital Economy, Peking University, Changsha, 410205, China^d College of Mechanics and Engineering Science, Hohai University, Nanjing, 210098, China

ARTICLE INFO

Keywords:

Asymptotic homogenization

Brittle fracture

Microcrack

Strain gradient

Strain rate

ABSTRACT

We develop an energetically consistent framework for modeling dynamic deformation and fracture of brittle materials, in which both the elastodynamic equation and the damage/fracture law are derived from the same ϵ^1 -order two-scale asymptotic approximation of the strain and kinetic energy functions, with strain gradient and strain rate effects naturally embedded. Based on these energy functions, Hamilton's principle is applied to derive a strain gradient elastodynamic equation that naturally accounts for damage-induced softening. Concurrently, applying the Griffith criterion yields a microcrack evolution equation driven by macroscopic strain, strain gradient, and strain rate. The resulting brittle fracture model is shown to rigorously satisfy the Clausius-Duhem inequality. Moreover, both the elastodynamic equation and the damage/fracture law are governed by a concise set of coefficients, formulated as integrals over microscopic cell functions that depend exclusively on intrinsic material parameters—namely the elastic moduli, microcrack size, and microcrack spacing.

Numerical simulations show that neglecting strain-gradient and strain-rate terms in the elastodynamic governing equations leads to unphysical phenomena such as infinite wave speeds at short wavelengths and stress singularities at macrocrack notch tips. In contrast, the present energetically consistent modeling approach effectively eliminates these spurious effects. Furthermore, simulations based on the proposed model quantitatively reproduce results from dynamic fracture experiments, including damage zone characteristics, free surface velocity profiles, and the strain-rate dependence of dynamic fracture strength.

1. Introduction

The early development of fracture mechanics, based on the pioneering works of Griffith (Griffith, 1921) and Irwin (Irwin, 1958), established the fundamental principle that crack propagation occurs when the energy release rate exceeds a critical threshold. This theoretical framework has since been widely applied to various fracture phenomena, including quasi-static (Yin et al., 2015) and dynamic (Bourdin et al., 2011) regimes, as well as thermodynamically consistent formulations (Rice, 1978; Cannizzo and Giordano, 2023).

Although Griffith's theory provides a solid foundation, it remains inherently macroscopic, focusing on the overall energy balance while neglecting the explicit role of microscopic mechanisms in governing fracture processes. Fracture is widely recognized as a complex, multi-scale phenomenon governed by microstructural features such as voids, defects, dislocations, and grain boundaries (Hahn, 1984). In brittle materials, microcracks are the primary microstructural features controlling macroscopic fracture behavior. Brittle fracture is primarily driven by the nucleation, growth, and coalescence of microcracks in the vicinity of the macrocrack tip under stress concentration (Ravi-Chandar and Yang, 1997). Furthermore, the characteristics of microcracks significantly influence macroscopic mechanical behavior, including stress-strain relations (Gross and Seelig, 2017) and wave dispersion phenomena (Gross and Zhang, 1992).

Capturing the effects of microcracks remains a central challenge in multi-scale damage modeling, due to the highly complex interactions between microcracks and externally applied loads (Mier and Vliet, 2003; Grassl et al., 2012; Z.P. and Planas, 2019). Over the past few decades, numerous studies have extended Griffith's framework by incorporating microcrack characteristics into fracture process modeling. For instance, Gambarotta

* Corresponding author.

E-mail address: xiang_meizhen@iapcm.ac.cn (M. Xiang).

and Lagomarsino (Gambarotta and Lagomarsino, 1993) proposed a model describing the behavior of brittle and quasi-brittle materials under both tensile and compressive loading, emphasizing the role of frictional interactions between microcrack faces. Rafiee et al. (Rafiee et al., 2004) demonstrated through numerical simulations that fracture toughness increases with crack speed, attributing this effect to microcrack nucleation ahead of the propagating macrocrack. Dascalu et al. (2008), Keita et al. (2014), Dascalu (2024) developed models based on two-scale asymptotic analysis and energy flux theory (the J-integral) to capture size effects on damage localization, fracture strength, and rate-dependent responses under dynamic loading. Collectively, these approaches have significantly advanced the understanding of fracture as a multi-scale phenomenon, underscoring the pivotal role of microstructural features in governing the macroscopic fracture behavior of materials.

When dominant microstructural length scales, such as microcrack sizes, become comparable to macroscopic dimensions, nonlocal interactions between microstructural features become significant (Smyshlyaev and Cherednichenko, 2000; Peerlings and Fleck, 2004; Lazar and Po, 2015). Classical continuum mechanics, which inherently assumes a local relationship between stress and strain, fails to capture these salient nonlocal effects. To account for such behaviors, strain gradient theories have been developed (Mindlin, 1965; Mindlin and Eshel, 1968; Toupin, 1962) and successfully applied across various disciplines, including elasticity (Aifantis, 2003; Lam et al., 2003), plasticity (Fleck et al., 1994; Gurtin, 2000; Jebahi and Forest, 2023; Amouzou-Adoun et al., 2024; Bacquaert et al., 2025), thermoelasticity (Ahmadi and Firoozbakhsh, 1975; Shishesaz et al., 2017), and anisotropic dispersive wave propagation (Bacigalupo and Gambarotta, 2014; Rosi and Auffray, 2016). Numerous studies have demonstrated the effectiveness of these theories in capturing microstructural effects (Nix and Gao, 1998; Aifantis, 1999; Liebold and Müller, 2015).

In the context of fracture mechanics, strain gradient models offer advantages beyond capturing nonlocal effects; they are also capable of smoothing out unphysical stress singularities that arise at crack tips in classical continuum mechanics (Aifantis, 1992; Gitman et al.; Askes and Aifantis, 2011). As a consequence, strain gradient models can provide numerical solutions that are less sensitive to mesh discretization (Hosseini and Niiranen, 2022). Given these advantages, various strain gradient fracture models have been proposed to enhance the understanding and prediction of fracture processes in materials. For instance, Li et al. (Li, 2011a; Li et al., 2011a) derived a strain gradient constitutive relation for a two-dimensional elastic material containing numerous microcracks and introduced a resistance curve to describe microcrack growth. Combining these elements, they formulated an energy potential to characterize the evolution of damage under applied loading. Martínez-Pañeda and Niordson (2016) developed a generalized approach for crack-tip analysis in strain gradient plasticity, emphasizing the crucial role of strain gradients under finite deformations. In addition, Nguyen and Niiranen (2020) recently proposed a nonlocal continuum damage model for micro-architected materials within the strain-gradient framework, implemented via isogeometric analysis, in which microstructure-specific length scales were introduced to capture material nonlocality and size effects.

Despite their significant success, strain gradient theories face a major challenge that limits their widespread application: the identification of higher-order material parameters associated with strain gradient and strain rate effects, which are notoriously difficult to measure experimentally. Considerable efforts over the past few decades have been devoted to determining these parameters through bottom-up multiscale techniques, which establish connections between strain gradient models and underlying microstructural features (Sunyk and Steinmann, 2003; Xiang et al., 2012; Admal et al., 2017; Drugan, 2000; Geers et al., 2001; Kouznetsova et al., 2002; Yvonnet et al., 2020). Among these techniques, asymptotic homogenization method – also referred to as two-scale asymptotic expansion or mathematical homogenization theory – has emerged as a powerful method for deriving strain gradient models for heterogeneous materials with periodic microstructures (Bensoussan et al., 1979; Oleinik et al., 1992; Terada and Kikuchi, 2001). This approach enables the systematic derivation of both microscopic and macroscopic governing equations, as well as the evaluation of localized behaviors arising from fine-scale heterogeneity (Terada and Kikuchi, 2001). It has been widely applied across various disciplines, including fracture mechanics (Triantafyllidis and Bardenhagen, 1996; Rao et al., 2022, 2023; Yang et al., 2023; You et al., 2025), scalar antiplane shear problems (Smyshlyaev and Cherednichenko, 2000), wave dispersion analysis (Chen and Fish, 2001; Bacigalupo and Gambarotta, 2012), and the mechanical characterization of hierarchical lattices (Yang et al., 2020, 2024). Moreover, asymptotic homogenization provides a rigorous framework for both the derivation and theoretical analysis of strain gradient models (Li et al., 2025).

A complete description of dynamic deformation and fracture requires both an elastodynamic governing equation and a damage/fracture law. Several studies (Placidi et al., 2018a; Placidi and Barchiesi, 2018; Placidi et al., 2018b, 2019; Makvandi et al., 2019; You et al., 2025) have incorporated strain gradient effects into both formulations, representing significant advancements beyond classical continuum approaches. As emphasized by Placidi et al. (2019), both the stiffness and the damage parameters are intrinsically linked to the underlying microstructure. However, in most of previous works, the model parameters are often separately described through unrelated phenomenological assumptions, lacking rigorous micro-mechanical foundation. Moreover, existing strain gradient fracture theories have primarily focused on quasi-static conditions, neglecting inertial and strain rate effects.

In our previous works, we developed a two-scale asymptotic homogenization approach for deriving strain-gradient brittle fracture models under both quasi-static (Rao et al., 2022) and dynamic conditions (Rao et al., 2023). In these studies, the homogenized elasticity governing equation and the damage/fracture law were constructed on different, and hence inconsistent, theoretical foundations. Specifically, the homogenized elasticity governing equation was obtained by directly integrating the coefficient of the ϵ^0 -order term (with ϵ denoting the microscopic representative volume element (RVE) length scale) in the asymptotic expansion of the microscopic governing equation. This procedure is equivalent to deriving the elasticity governing equation from the ϵ^0 -order approximation of the strain and kinetic energies. In contrast, the damage/fracture law was derived from the ϵ^1 -order approximation of these energy functions. As a result, an energetic inconsistency arises between the two formulations.

To eliminate this inconsistency, in the present work, we develop an energetically consistent framework for modeling dynamic deformation and fracture of brittle materials, in which both the elastodynamic equation and the damage/fracture law are derived from the same ϵ^1 -order approximation of the strain and kinetic energies. First, the homogenized strain and kinetic energy functions of the microscopic RVE with embedded microcracks are derived, with strain gradient and strain rate effects naturally embedded. Based on these energy functions, Hamilton's principle is employed to derive a strain gradient elastodynamic model that captures damage-induced softening. Meanwhile, the Griffith criterion is applied to obtain a microcrack evolution equation governed by macroscopic strain, strain gradient, and strain rate. The resulting elastodynamic and damage/fracture formulations share a concise set of coefficients, expressed as integrals over microscopic cell functions that depend solely on the elastic moduli and microcrack size and spacing. This two-scale framework establishes an energetically consistent micromechanical linkage between microscale features and macroscale dynamic deformation and fracture. It embeds strain-gradient and strain-rate effects in both the elastodynamic equation and the damage/fracture law, and is proved to rigorously satisfy the Clausius–Duhem inequality.

Extensive numerical simulations are conducted to demonstrate the model's capability in capturing several key mechanical behaviors, with particular emphasis on the coupled effects of microstructural size, macroscopic strain gradients, and strain rates on fracture strength, the brittle-ductile transition, and wave dispersion. These simulations reveal that energetically inconsistent models, which omit strain-gradient and strain-rate

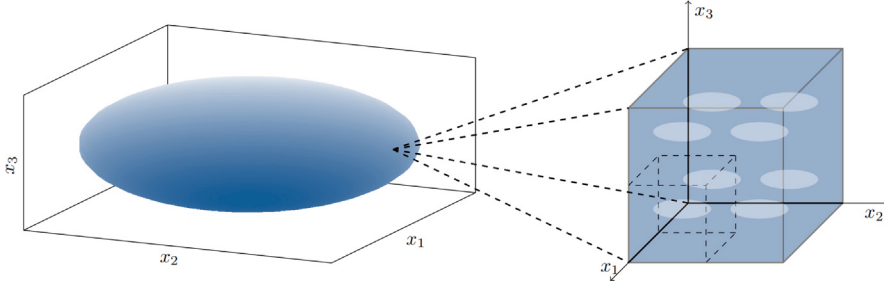


Fig. 1. Periodic assumption of the microcrack distribution within the RVE.

contributions in the elastodynamic governing equations, give rise to unphysical phenomena such as infinite wave speeds at short wavelengths and stress singularities at macrocrack notch tips. By contrast, the present energetically consistent formulation effectively eliminates these spurious effects. Moreover, results obtained from simulations based on the proposed model quantitatively reproduce observations from dynamic fracture experiments, including damage zone morphology, free-surface velocity profiles, and the strain-rate dependence of fracture strength, thereby demonstrating the model's predictive fidelity.

The organization of this paper is as follows: In Section 2, a two-scale framework incorporating the effects of microcracks is developed to derive the homogenized strain energy and kinetic energy densities. Section 3 provides a rigorous derivation of the strain gradient elastodynamic equation. In Section 4, a dynamic damage model for microcrack propagation and macro-scale fracture is formulated. Section 5 presents numerical results for both the single-element analysis and the macro-scale structural response to validate the predictive capability of the proposed model. Finally, the conclusions are drawn in Section 6. Throughout this paper, the Einstein summation convention for repeated indices is adopted, and all subscripts and superscripts in this paper can take values 1, 2, 3.

2. Homogenized energy functions based on two-scale asymptotic analysis

We consider a bounded elastic solid Ω in three-dimensional space, where microscopic cracks are randomly distributed at each macroscopic point. For tractability, these microcracks are idealized as penny-shaped and arranged in a locally periodic pattern, a widely adopted approximation (Dascalu et al., 2008; Dascalu, 2024) that captures the essential effects of microcrack area and spacing while reducing modeling complexity, as illustrated in Fig. 1. The average distance between two adjacent microcracks is denoted by ϵ , which also represents the periodicity of the crack arrangement. A periodic representative volume element (RVE), denoted by Y_ϵ , is selected with dimensions $\epsilon \times \epsilon \times \epsilon$, such that a microcrack C_ϵ is centered within the RVE. The radius of the microcrack is denoted by $r \in [0, \frac{\epsilon}{2}]$, and the corresponding crack surface area is $s = \pi r^2$.

To characterize the geometry of the microcracks in a dimensionless manner, we define the normalized microcrack radius as $R = \frac{r}{\epsilon} \in [0, \frac{1}{2}]$, and the normalized microcrack area as $S = \pi R^2 \in [0, \frac{\pi}{4}]$. In the present work, the variable S serves as the damage variable, interpolating between the unbroken ($S = 0$) and fully broken ($S = \frac{\pi}{4}$) states of the material.

In the solid region $Y_\epsilon = Y_\epsilon \setminus C_\epsilon$ of the RVE, the material response is assumed to be linear elastic. The displacement field \mathbf{u}^ϵ satisfies the following elastodynamic equations:

$$\rho \ddot{\mathbf{u}} = \frac{\partial \sigma_{ij}^\epsilon}{\partial x_j} + f_i, \quad \sigma_{ij}^\epsilon = C_{ijkl} e_{kl}(\mathbf{u}^\epsilon), \quad e_{kl}(\mathbf{u}^\epsilon) = \frac{1}{2} \left(\frac{\partial u_k^\epsilon}{\partial x_j} + \frac{\partial u_j^\epsilon}{\partial x_k} \right), \quad (1)$$

where \mathbf{u}^ϵ , $e_{ij}(\mathbf{u}^\epsilon)$, and σ^ϵ represent the displacement, strain, and stress fields within the RVE, respectively.

In this study, we assume that the microcracks can only undergo extension, without any closure. Therefore, the stress field σ and the displacement field \mathbf{u}^ϵ must satisfy the following boundary conditions on the crack surface C_ϵ :

$$\sigma^\epsilon \cdot \mathbf{n} = 0, \quad [\mathbf{u}^\epsilon \cdot \mathbf{n}] > 0, \quad (2)$$

where \mathbf{n} is the outward normal vector on the crack surface, and $[\cdot]$ denotes the jump across the crack surface.

To analyze the material response at different scales, we apply the scaling transformation $\mathbf{y} = \mathbf{x}/\epsilon$, mapping the periodic RVE, Y_ϵ , onto the normalized reference cell $Y = [0, 1] \times [0, 1] \times [0, 1]$, as illustrated in Fig. 2. The normalized crack is denoted by C , with a scaled crack area $S = s/\epsilon^2$. The upper and lower surfaces of the crack are represented as C^+ and C^- , respectively, while the solid region is denoted by $Y_s = Y \setminus C$.

With two scales, macroscopic (\mathbf{x}) and microscopic (\mathbf{y}), the differentiation chain rule is expressed as:

$$\frac{d}{dx} = \frac{\partial}{\partial x} + \frac{1}{\epsilon} \frac{\partial}{\partial y}. \quad (3)$$

The displacement field \mathbf{u}^ϵ is expanded as a power series in ϵ following the method of asymptotic homogenization (Bakhvalov and Panasenko, 1989):

$$\mathbf{u}^\epsilon(\mathbf{x}) = \mathbf{u}^{(0)}(\mathbf{x}) + \sum_{i=1}^{\infty} \epsilon^i \mathbf{u}^{(i)}(\mathbf{x}, \mathbf{y}), \quad (4)$$

where $\mathbf{u}^{(i)}(\mathbf{x}, \mathbf{y})$ ($i \in \mathbb{N}$) are Y -periodic functions of the microscopic variable \mathbf{y} .

To simplify the analysis, we define the Sobolev space:

$$D(Y_s) = \left\{ \mathbf{v} \mid \mathbf{v} \in [H^1(Y_s)]^3, \mathbf{v} \text{ is } Y\text{-periodic in } \mathbf{y}, \int_Y \mathbf{v} d\mathbf{y} = 0 \right\}. \quad (5)$$

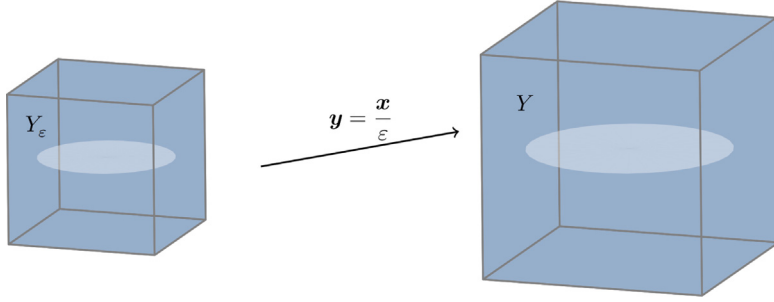


Fig. 2. Scaling transformation from the periodic RVE Y_ϵ to the normalized reference cell Y .

By substituting the expansion (4) into the elastodynamic Eqs. (1) and collecting terms of the same order in ϵ , we derive the governing equations for $\mathbf{u}^{(0)}, \mathbf{u}^{(1)}, \mathbf{u}^{(2)}$:

$$\begin{cases} \frac{\partial}{\partial y_j} [C_{ijkl} e_{ykl}(\mathbf{u}^{(0)})] = 0, \\ \frac{\partial}{\partial y_j} [C_{ijkl} (e_{xkl}(\mathbf{u}^{(0)}) + e_{ykl}(\mathbf{u}^{(1)}))] = 0, \end{cases} \quad (6a)$$

$$\begin{cases} \frac{\partial}{\partial y_j} [C_{ijkl} (e_{xkl}(\mathbf{u}^{(1)}) + e_{ykl}(\mathbf{u}^{(2)}))] + \frac{\partial}{\partial x_j} [C_{ijkl} (e_{xkl}(\mathbf{u}^{(0)}) + e_{ykl}(\mathbf{u}^{(1)}))] + f_i = \rho \ddot{u}_i^{(0)}. \end{cases} \quad (6c)$$

$$\begin{cases} C_{ijkl} (e_{xkl}(\mathbf{u}^{(0)}) + e_{ykl}(\mathbf{u}^{(1)})) n_j = 0, & \text{on } C^\pm, \\ C_{ijkl} (e_{xkl}(\mathbf{u}^{(1)}) + e_{ykl}(\mathbf{u}^{(2)})) n_j = 0, & \text{on } C^\pm. \end{cases} \quad (7)$$

The corresponding boundary conditions on C^\pm are given by:

From Eq. (6a), it follows that $\mathbf{u}^{(0)}(\mathbf{x}, \mathbf{y}) = \mathbf{u}^{(0)}(\mathbf{x})$, which is independent of \mathbf{y} (cf. Bakhvalov and Panasenko, 1989). In this work, $\mathbf{u}^{(0)}(\mathbf{x})$ is chosen as the approximation for the macroscopic displacement field. From Eqs. (6b) and (6c), the displacement fields $\mathbf{u}^{(1)}$ and $\mathbf{u}^{(2)}$, which belong to the $D(Y_s)$, are expressed as:

$$\mathbf{u}^{(1)}(\mathbf{x}, \mathbf{y}) = \mathbf{N}^{pq}(\mathbf{y}) e_{xpq}(\mathbf{u}^{(0)})(\mathbf{x}) + \tilde{\mathbf{u}}^{(1)}(\mathbf{x}), \quad \mathbf{u}^{(2)}(\mathbf{x}, \mathbf{y}) = \mathbf{N}^{pqr}(\mathbf{y}) e_{x, pqr}(\mathbf{u}^{(0)})(\mathbf{x}) + \tilde{\mathbf{u}}^{(2)}(\mathbf{x}), \quad (8)$$

where $\mathbf{N}^{pq}, \mathbf{N}^{pqr} \in D(Y_s)$ are the first- and second-order cell functions, respectively, which satisfy the following equations:

$$\begin{cases} \frac{\partial}{\partial y_j} [C_{ijkl} e_{ykl}(\mathbf{N}^{pq}) + C_{ijpq}] = 0, & \text{in } Y_s, \\ (C_{ijkl} e_{ykl}(\mathbf{N}^{pq}) + C_{ijpq}) n_j = 0, & \text{on } C^\pm, \end{cases} \quad (9)$$

and

$$\begin{cases} \frac{\partial}{\partial y_j} [C_{ijkl} e_{ykl}(\mathbf{N}^{pqr}) + C_{ijkr} N_k^{pq}] + C_{irpq} + C_{irk} e_{ykl}(\mathbf{N}^{pq}) = \hat{C}_{irpq}, & \text{in } Y_s, \\ (C_{ijkl} e_{ykl}(\mathbf{N}^{pqr}) + C_{ijkr} N_k^{pq}) n_j = 0, & \text{on } C^\pm. \end{cases} \quad (10)$$

Here, $\hat{C}_{ijkl} = \int_Y C_{ijkl} + C_{ijpq} e_{ypq}(\mathbf{N}^{kl}) d\mathbf{y}$. $e_{xpq}(\mathbf{u}^{(0)})$ and $e_{x, pqr}(\mathbf{u}^{(0)})$ are the strain and strain gradient associated with the leading-order displacement field $\mathbf{u}^{(0)}$, defined as:

$$e_{xpq}(\mathbf{u}^{(0)}) = \frac{1}{2} \left(\frac{\partial u_p^{(0)}}{\partial x_q} + \frac{\partial u_q^{(0)}}{\partial x_p} \right), \quad e_{x, pqr} = \frac{1}{2} \left(\frac{\partial^2 u_p^{(0)}}{\partial x_q \partial x_r} + \frac{\partial^2 u_q^{(0)}}{\partial x_p \partial x_r} \right). \quad (11)$$

The terms $\tilde{\mathbf{u}}^{(1)}$ and $\tilde{\mathbf{u}}^{(2)}$ in Eq. (8) are integration constants. We impose the additional conditions

$$\int_{Y_s} \mathbf{u}^{(1)} d\mathbf{y} = \int_{Y_s} \mathbf{u}^{(2)} d\mathbf{y} = \mathbf{0},$$

which immediately yields $\tilde{\mathbf{u}}^{(1)} = \tilde{\mathbf{u}}^{(2)} = \mathbf{0}$.

Then, the first-order approximation of the strain field in Y_ϵ is expressed as:

$$\begin{aligned} e_{ij}(\mathbf{u}^\epsilon) &\approx [e_{xij}(\mathbf{u}^{(0)}) + e_{yij}(\mathbf{u}^{(1)})] + \epsilon [e_{xij}(\mathbf{u}^{(1)}) + e_{yij}(\mathbf{u}^{(2)})] \\ &= [e_{xij}(\mathbf{u}^{(0)}) + e_{yij}(\mathbf{N}^{pq}) e_{xpq}(\mathbf{u}^{(0)})] \\ &\quad + \epsilon \left[\frac{1}{2} \left(N_i^{pq} e_{xpqj}(\mathbf{u}^{(0)}) + N_j^{pq} e_{xpqi}(\mathbf{u}^{(0)}) \right) + e_{yij}(\mathbf{N}^{pqr}) e_{x, pqr}(\mathbf{u}^{(0)}) \right]. \end{aligned} \quad (12)$$

The corresponding approximation of the strain energy is given by:

$$\begin{aligned}
 w^e &= \frac{1}{|Y_{s_\epsilon}|} \int_{Y_{s_\epsilon}} \frac{1}{2} C_{ijkl} e_{ij}(\mathbf{u}^\epsilon) e_{kl}(\mathbf{u}^\epsilon) d\mathbf{x} \\
 &= \frac{1}{2\epsilon^2} \int_{Y_{s_\epsilon}} C_{ijkl} [e_{xij}(\mathbf{u}^{(0)}) + e_{yij}(\mathbf{u}^{(1)})] [e_{xkl}(\mathbf{u}^{(0)})] d\mathbf{x} \\
 &\quad + \frac{1}{2\epsilon^2} \int_{Y_{s_\epsilon}} C_{ijkl} [e_{xij}(\mathbf{u}^{(0)}) + e_{yij}(\mathbf{u}^{(1)})] [e_{ykl}(\mathbf{u}^{(1)}) + 2\epsilon e_{ykl}(\mathbf{u}^{(2)})] d\mathbf{x} \\
 &\quad + \frac{1}{2\epsilon^2} \int_{Y_{s_\epsilon}} C_{ijkl} [e_{xij}(\mathbf{u}^{(0)}) + e_{yij}(\mathbf{u}^{(1)})] [2\epsilon e_{xkl}(\mathbf{u}^{(1)})] d\mathbf{x} \\
 &\quad + \frac{1}{2} \int_{Y_{s_\epsilon}} C_{ijkl} e_{xij}(\mathbf{u}^{(1)}) e_{xkl}(\mathbf{u}^{(1)}) d\mathbf{x} + \int_{Y_{s_\epsilon}} C_{ijkl} e_{xij}(\mathbf{u}^{(1)}) e_{ykl}(\mathbf{u}^{(2)}) d\mathbf{x} + \frac{1}{2} \int_{Y_{s_\epsilon}} C_{ijkl} e_{yij}(\mathbf{u}^{(2)}) e_{ykl}(\mathbf{u}^{(2)}) d\mathbf{x} \\
 &= \frac{1}{2} \hat{C}_{ijkl} \mathcal{E}_{ij} \mathcal{E}_{kl} + \epsilon \hat{G}_{ijklm} \mathcal{E}_{ij} \mathcal{E}_{klm} + \frac{\epsilon^2}{2} \hat{D}_{ijklmn} \mathcal{E}_{ij,k} \mathcal{E}_{lm,n},
 \end{aligned} \tag{13}$$

where $\mathcal{E}_{ij} = \langle e_{xij}(\mathbf{u}^{(0)}) \rangle$, $\mathcal{E}_{ij,k} = \langle e_{xijk}(\mathbf{u}^{(0)}) \rangle$ represent the homogenized strain and strain gradient. \hat{C}_{ijkl} , \hat{G}_{pqmn} , \hat{D}_{ijklmn} represent the homogenized material parameters and are defined by:

$$\left\{ \begin{array}{l} \hat{C}_{ijkl} = \int_{Y_s} C_{ijkl} + C_{ijpq} e_{ypq}(\mathbf{N}^{kl}) d\mathbf{y}, \end{array} \right. \tag{14a}$$

$$\left\{ \begin{array}{l} \hat{G}_{pqmn} = \int_{Y_s} (C_{pqkl} + C_{ijkl} \mathbf{N}_{i,j}^{pq}) \mathbf{N}_k^{mn} d\mathbf{y}, \end{array} \right. \tag{14b}$$

$$\left\{ \begin{array}{l} \hat{D}_{ijklmn} = \int_{Y_s} C_{pkqn} \mathbf{N}_p^{ij} \mathbf{N}_q^{lm} + C_{pqrs} e_{ypq}(\mathbf{N}^{ijk}) e_{yrs}(\mathbf{N}^{lmn}) d\mathbf{y}. \end{array} \right. \tag{14c}$$

In deriving Eq. (18), we adopt the following equation:

$$\int_{Y_s} (C_{ijpq} + C_{ijkl} e_{ykl}(\mathbf{N}^{pq})) e_{yij}(\mathbf{v}) d\mathbf{y} = 0, \quad \forall \mathbf{v} \in D(Y_s), \tag{15}$$

which arises from the weak form of the first-order cell function $\mathbf{N}^{pq}(\mathbf{y})$ (see Eq. (9)).

Following a similar procedure, we obtain the homogenized kinetic energy density function with the first-order truncation of the displacement field \mathbf{u}^ϵ as:

$$\begin{aligned}
 w^k &= \frac{1}{|Y_{s_\epsilon}|} \int_{Y_{s_\epsilon}} \frac{1}{2} \rho \frac{\partial \mathbf{u}^\epsilon}{\partial t} \frac{\partial \mathbf{u}^\epsilon}{\partial t} d\mathbf{x} \\
 &= \frac{1}{2} \hat{\rho} \dot{u}_i \dot{u}_i + \epsilon H_{ijk} \dot{u}_k \dot{\mathcal{E}}_{ij} + \frac{\epsilon^2}{2} F_{ijkl} \dot{\mathcal{E}}_{ij} \dot{\mathcal{E}}_{kl},
 \end{aligned} \tag{16}$$

where $\dot{u}_i = \left\langle \frac{\partial u^0}{\partial t} \right\rangle$, $\dot{\mathcal{E}}_{ij} = \left\langle \frac{\partial e_{xij}(\mathbf{u}^{(0)})}{\partial t} \right\rangle$ represent the homogenized velocity and strain rate respectively. And $\hat{\rho}$, \hat{H}_{ijk} and \hat{F}_{ijkl} represent the homogenized material parameters, defined as :

$$\left\{ \begin{array}{l} \hat{\rho} = \int_{Y_s} \rho d\mathbf{y} = \rho, \end{array} \right. \tag{17a}$$

$$\left\{ \begin{array}{l} \hat{H}_{ijk} = \int_{Y_s} \rho \mathbf{N}_k^{ij} d\mathbf{y}, \end{array} \right. \tag{17b}$$

$$\left\{ \begin{array}{l} \hat{F}_{ijkl} = \int_{Y_s} \rho \mathbf{N}_p^{ij} \mathbf{N}_p^{kl} d\mathbf{y}. \end{array} \right. \tag{17c}$$

A comprehensive derivation of this result is provided in Li et al. (2025).

Furthermore, exploiting the central symmetry of the penny-shaped microcrack structure, it can be rigorously demonstrated that $\hat{\mathbf{G}} = \mathbf{0}$ and $\hat{\mathbf{H}} = \mathbf{0}$, as shown in Li et al. (2025). Therefore, the simplified expressions for the strain energy density and kinetic energy density are given by¹:

$$w^e = \frac{1}{2} \hat{C}_{ijkl} \mathcal{E}_{ij} \mathcal{E}_{kl} + \frac{\epsilon^2}{2} \hat{D}_{ijklmn} \mathcal{E}_{ij,k} \mathcal{E}_{lm,n}, \tag{18}$$

$$w^k = \frac{1}{2} \hat{\rho} \dot{u}_i \dot{u}_i + \frac{\epsilon^2}{2} \hat{F}_{ijkl} \dot{\mathcal{E}}_{ij} \dot{\mathcal{E}}_{kl}. \tag{19}$$

The first term in w^e represents the elastic energy stored due to macroscopic deformation, while the second term accounts for additional stored energy related to microscopic inhomogeneous deformation arising from microstructural heterogeneities. Similarly, in the homogenized kinetic energy function w^k , the first term represents the kinetic energy associated with macroscopic motion and deformation, while the second term captures the contribution from microscopic fluctuations of velocity field induced by local heterogeneities. Such separation clarifies the contribution of each mechanism to the overall energy landscape.

¹ These expressions are equivalent to second-order approximation of the homogenized strain and kinetic energy densities (Li et al., 2025).

Remark 1. The assumptions $\hat{\mathbf{G}} = 0$ and $\hat{\mathbf{H}} = 0$ correspond to a centro-symmetric microcrack distribution within the RVE. When this symmetry is absent, however, the corresponding $\hat{\mathbf{G}}$ and $\hat{\mathbf{H}}$ terms should be retained. Notably, the inclusion of $\hat{\mathbf{G}}$ is essential for capturing specific physical phenomena in materials with non-centro-symmetric microstructures, both under quasi-static conditions (Poncelet et al., 2018) and in dynamic problems (Toupin, 1962; Maranganti and Sharma, 2007). Moreover, asymptotic analysis has shown that the influence of $\hat{\mathbf{G}}$ may even dominate over that of $\hat{\mathbf{D}}$ (Boutin, 1996).

Retaining these terms does not introduce essential difficulty into the present theoretical framework. Actually, In a recent work of the authors (Li et al., 2025), we have explored extended energy functionals that incorporate such terms as well as higher-order contributions to construct elastodynamics governing equations.

In the strain gradient elasticity framework, the external potential work is typically expressed as:

$$W^{\text{ext}}(\mathbf{u}) = \int_{\Omega} f_k u_k \, d\mathbf{x} + \int_{\partial\Omega} g_k u_k \, dA + \int_{\partial\Omega} r_k D(u_k) \, dA + \sum_m \oint_{C_m} p_k u_k \, dr, \quad (20)$$

where f_k , g_k , r_k , and p_k represent the external force densities on the body and its boundaries. The surface gradient D_j and normal gradient D are defined as:

$$D_j = (\delta_{jk} - n_j n_k) \frac{\partial}{\partial x_k}, \quad D = n_k \frac{\partial}{\partial x_k}, \quad (21)$$

with \mathbf{n} being the unit normal on $\partial\Omega$. The boundary surface $\partial\Omega$ is divided into m smooth parts $\partial\Omega_n$, each bounded by an edge C_n with a surface unit vector k_n normal to the edge. The number of sharp edges is denoted by m .

3. Strain gradient elastodynamics model

Given the strain energy density w^e (Eq. (18)), kinetic energy density w^k (Eq. (19)), external potential work $W^{\text{ext}}(\mathbf{u})$ (Eq. (20)), the boundary condition $\mathbf{u} = \bar{\mathbf{u}}$ on $\Gamma \subset \partial\Omega$, the initial conditions $\mathbf{u}(\mathbf{x}, 0) = \mathbf{u}_0(\mathbf{x})$ and $\dot{\mathbf{u}}(\mathbf{x}, 0) = \mathbf{u}_1(\mathbf{x})$ in Ω , and the initial damage distribution $S(\mathbf{x}, 0) = S_0(\mathbf{x}) \in [0, \frac{\pi}{4}]$ for $\mathbf{x} \in \Omega$, the displacement field \mathbf{u} is governed by the strain gradient elastodynamics equation derived from Hamilton's principle.

Hamilton's principle states that the dynamics of an elastic system are determined by a variational problem for the Lagrangian functional, which, when applied to the homogenized medium Ω for an arbitrary independent variation $\delta\mathbf{u}$, is expressed as:

$$\delta \int_{t_0}^{t_1} \int_{\Omega} (w^k - w^e) \, d\mathbf{x} dt + \delta \int_{t_0}^{t_1} W^{\text{ext}} \, dt = 0. \quad (22)$$

By applying the divergence theorem, the variation of the total kinetic energy can be expressed as:

$$\begin{aligned} \delta \int_{t_0}^{t_1} \int_{\Omega} w^k \, d\mathbf{x} dt &= \int_{t_0}^{t_1} \int_{\Omega} \frac{\partial w^k}{\partial \dot{u}_i} \delta \dot{u}_i + \frac{\partial w^k}{\partial \dot{\mathcal{E}}_{ij}} \delta \dot{\mathcal{E}}_{ij} \, d\mathbf{x} dt \\ &= - \int_{t_0}^{t_1} \int_{\Omega} \dot{\rho} \ddot{u}_i \delta u_i - \varepsilon^2 \hat{F}_{ijkl} \ddot{\mathcal{E}}_{kl,j} \delta u_l \, d\mathbf{x} dt - \int_{t_0}^{t_1} \int_{\partial\Omega} \varepsilon^2 \hat{F}_{ijkl} \left(\frac{\partial \ddot{u}_l}{\partial x_k} \right) n_j \delta u_l \, dAdt. \end{aligned} \quad (23)$$

To address the variation of strain energy, we first define the stress tensor Σ_{ij} and the double stress tensor Γ_{ijk} as the energy conjugates of the strain and its gradient, respectively:

$$\Sigma_{ij} = \frac{\partial w^e}{\partial \mathcal{E}_{ij}} = \hat{C}_{ijkl} \mathcal{E}_{kl}, \quad \Gamma_{ijk} = \frac{\partial w^e}{\partial \mathcal{E}_{ijk,k}} = \varepsilon^2 \hat{B}_{ijklmn} \mathcal{E}_{lm,n}. \quad (24)$$

These are referred to as higher-order effective constitutive relations.

Then, by applying the Green's divergence theorem and Stokes' surface divergence theorem, the variation of the total strain energy is given by:

$$\begin{aligned} \delta \int_{\Omega} w^e \, d\mathbf{x} dt &= \int_{\Omega} \Sigma_{ij} \delta \mathcal{E}_{ij} + \Gamma_{ijk} \delta \mathcal{E}_{ijk} \, d\mathbf{x} dt \\ &= - \int_{\Omega} \left(\frac{\partial}{\partial x_i} \Sigma_{ik} - \frac{\partial^2}{\partial x_i x_j} \Gamma_{ijk} \right) \delta u_k \, d\mathbf{x} \\ &\quad + \int_{\partial\Omega} \left\{ \left[n_j (\Sigma_{ij} - \frac{\partial \Gamma_{ijk}}{\partial x_i}) + n_i n_j \Gamma_{ijk} (D_l n_l) - D_j (n_i \Gamma_{ijk}) \right] \delta u_k + n_i n_j \Gamma_{ijk} D \delta u_k \right\} \, dA \\ &\quad + \sum_m \oint_{C_m} [n_i k_j \Gamma_{ijk}] \delta u_k \, dr, \end{aligned} \quad (25)$$

where m is the number of sharp edges, and $[\cdot]$ represents the difference between the bracketed terms on the two sides of the edge (following Lam et al. (2003)).

The variation of external potential work is given by:

$$\delta W^{\text{ext}} = \int_{\Omega} f_k \delta u_k \, d\mathbf{x} + \int_{\partial\Omega} g_k \delta u_k \, dA + \int_{\partial\Omega} r_k D(\delta u_k) \, dA + \sum_m \oint_{C_m} p_k \delta u_k \, dr. \quad (26)$$

Thus, by substituting Eqs. (23) to (26) into Eq. (22), and noting the arbitrariness of $\delta\mathbf{u}$, we obtain the following strain gradient elastodynamics equations:

$$\left\{ \begin{array}{l} \hat{\rho}\ddot{\mathbf{u}}_i - \varepsilon^2 \hat{F}_{ijkl} \ddot{\mathcal{E}}_{kl,j} - \frac{\partial}{\partial x_j} (\Sigma_{ij}) + \varepsilon^2 \frac{\partial^2}{\partial x_k \partial x_j} (\Gamma_{ijk}) = f_i, \text{ in } \Omega, \\ \mathbf{u} = \bar{\mathbf{u}} \text{ or } n_j (\Sigma_{ij} - \frac{\partial \Gamma_{ijk}}{\partial x_i}) + n_i n_j \Gamma_{ijk} (\mathcal{D}_l n_l) - \mathcal{D}_j (n_i \Gamma_{ijk}) + \varepsilon^2 \hat{F}_{ijkl} \left(\frac{\partial \ddot{\mathbf{u}}_i}{\partial x_j} \right) n_l = g_k, \text{ on } \partial\Omega, \end{array} \right. \quad (27a)$$

$$\left\{ \begin{array}{l} \frac{\partial \mathbf{u}}{\partial n} = \frac{\partial \bar{\mathbf{u}}}{\partial n} \text{ or } n_i n_j \Gamma_{ijk} = r_i, \text{ on } \partial\Omega, \\ \mathbf{u} = \bar{\mathbf{u}} \text{ or } [n_i k_j \Gamma_{ijk}] = p_k, \text{ on } C_m, \end{array} \right. \quad (27c)$$

$$\left\{ \begin{array}{l} \mathbf{u}|_{t=0} = \mathbf{u}_0, \quad \dot{\mathbf{u}}|_{t=0} = \mathbf{u}_1, \text{ in } \Omega. \end{array} \right. \quad (27e)$$

For the quasi-static fracture problem, the governing equations for \mathbf{u} in strain gradient elasticity are derived by neglecting the time-dependent terms in Eq. (27):

$$\left\{ \begin{array}{l} -\frac{\partial}{\partial x_j} (\Sigma_{ij}) + \varepsilon^2 \frac{\partial^2}{\partial x_k \partial x_j} (\Gamma_{ijk}) = f_i, \quad \text{in } \Omega, \\ \mathbf{u} = \bar{\mathbf{u}} \text{ or } n_j \left(\Sigma_{ij} - \frac{\partial \Gamma_{ijk}}{\partial x_i} \right) + n_i n_j \Gamma_{ijk} (\mathcal{D}_l n_l) - \mathcal{D}_j (n_i \Gamma_{ijk}) = g_k, \quad \text{on } \partial\Omega, \end{array} \right. \quad (28a)$$

$$\left\{ \begin{array}{l} \frac{\partial \mathbf{u}}{\partial n} = \frac{\partial \bar{\mathbf{u}}}{\partial n} \text{ or } n_i n_j \Gamma_{ijk} = r_k, \quad \text{on } \partial\Omega, \\ \mathbf{u} = \bar{\mathbf{u}} \text{ or } [n_i k_j \Gamma_{ijk}] = p_k, \quad \text{on } C_m. \end{array} \right. \quad (28d)$$

Remark 2. For a general isotropic elastic material, for which C_{ijkl} is symmetric and positive definite, we show that the fourth-order tensor \hat{C}_{ijkl} , \hat{F}_{ijkl} and the sixth-order tensor \hat{D}_{ijklmn} are all symmetric and positive definite in Appendix A. This guarantees the well-posedness of Eqs. (27), (28) (Niiranen et al., 2016; Hosseini and Niiranen, 2022; Li et al., 2025).

4. Strain gradient dynamic damage model

In this section, we formulate the evolution law for the damage variable $S(\mathbf{x}, t) \in [0, \frac{\pi}{4}]$, which incorporates strain effects, strain gradient effects, strain rate effects, and the microstructural features.

Firstly, the evolution of damage variable must satisfy the irreversibility condition:

$$\dot{S}(\mathbf{x}, t) \geq 0, \quad \forall \mathbf{x} \in \Omega, \quad (29)$$

ensuring that damage can only accumulate over time, reflecting the irreversible nature of the damage process.

Building upon the classical fracture theories developed by Griffith (Griffith, 1921) and Irwin (Irwin, 1957), crack propagation is triggered when the energy available for crack growth exceeds the energy required to create new crack surfaces. Applied to the microscopic RVE (Y_ϵ), this criterion implies that microcracks initiate propagation when the energy release rate G reaches a critical threshold G_c .

Under dynamic loading conditions, considering a stationary microcrack (i.e., a microcrack with zero propagation velocity), the energy release rate at a material point \mathbf{x} is given by:

$$\begin{aligned} G^{st}(\mathbf{u}, S; \mathbf{x}) &= -|Y_\epsilon| \frac{\partial(w^e + w^k)}{\partial s} = -\varepsilon^3 \frac{\partial(w^e + w^k)}{\partial s} = -\varepsilon \frac{\partial(w^e + w^k)}{\partial S} \\ &= - \left\{ \frac{\varepsilon}{2} \frac{\partial \hat{C}_{ijkl}(S)}{\partial S} \mathcal{E}_{ij} \mathcal{E}_{kl} + \frac{\varepsilon^3}{2} \frac{\partial \hat{D}_{ijklmn}(S)}{\partial S} \mathcal{E}_{ij,k} \mathcal{E}_{lm,n} + \frac{\varepsilon^3}{2} \frac{\partial \hat{F}_{ijkl}(S)}{\partial S} \dot{\mathcal{E}}_{ij} \dot{\mathcal{E}}_{kl} \right\}. \end{aligned} \quad (30)$$

When $G^{st} > G_c$, the microcrack becomes unstable and initiates propagation. For a microcrack propagating at a finite velocity \dot{r} , the dynamic energy release rate can be approximated as (Freund, 1990):

$$G = \left(1 - \frac{\dot{r}}{C_R} \right) G^{st} = \left(1 - \varepsilon \frac{\dot{S}}{\sqrt{4\pi S} C_R} \right) G^{st}, \quad (31)$$

where C_R denotes the Rayleigh wave speed, and the relation $S = \pi R^2 = \pi r^2/\varepsilon^2$ has been used.

By combining the expression for the dynamic energy release rate (Eq. (31)), the Griffith fracture criterion, and the irreversibility condition (Eq. (29)), we derive the following damage evolution equation

$$\dot{S} = \begin{cases} \frac{1}{\varepsilon} \sqrt{4\pi S} C_R \left(1 - \frac{G_c}{G^{st}} \right), & \text{if } G^{st} > G_c, \\ 0, & \text{if } G^{st} \leq G_c. \end{cases} \quad (32)$$

For quasi-static fracture problem, where the kinetic energy can be neglected, the energy release rate is given by

$$G^{static} = -\frac{\varepsilon}{2} \frac{\partial \hat{C}_{ijkl}(S)}{\partial S} \mathcal{E}_{ij} \mathcal{E}_{kl} - \frac{\varepsilon^3}{2} \frac{\partial \hat{D}_{ijklmn}(S)}{\partial S} \mathcal{E}_{ij,k} \mathcal{E}_{lm,n}. \quad (33)$$

Crack propagation is assumed to occur instantaneously relative to the timescale of external loading. Accordingly, once a microcrack becomes unstable (i.e., when $G^{static} \geq G_c$), it is assumed to traverse the entire RVE instantaneously, leading to an abrupt increase in the damage variable from its initial value S_0 to $S = \pi/4$.

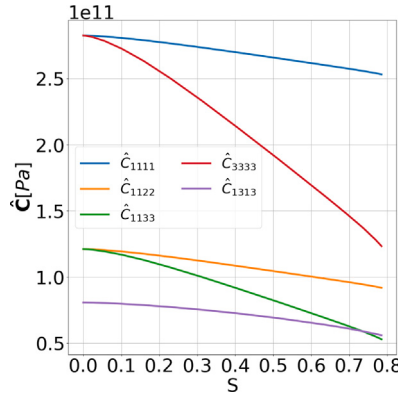


Fig. 3. Variation of the homogenized parameters \hat{C}_{ijkl} with the damage variable S .

Remark 3. Dascalu (2024) derived a damage evolution law based on the first-order two-scale asymptotic approximation of strain field and the J-integral method. Our work is distinct from Dascalu (2024) in several aspects. First of all, our approach is grounded in the homogenization of strain energy and kinetic energy instead of the J-integral. Our approach allows for constructing not only the damage law but also the elastodynamic governing equation based on unified energy functions. Moreover, while Dascalu (2024) essentially adopt a first-order approximation of the strain field which cannot account for strain gradient effects, our formulation incorporates higher-order truncations of the strain field and displacement field, enabling the model to capture strain gradient and strain rate effects in both the damage law and the elastodynamic governing equation.

Remark 4. If the strain-gradient and strain-rate terms in the governing equations of the displacement field, Eq.(27) and Eq.(28), are neglected, the system reduces to the classical homogenized formulation. In this case, the fracture model degenerates into the framework previously established in Rao et al. (2022, 2023), where the displacement equation is obtained from the ϵ^0 -order approximation of the energy functions, while the damage/fracture law is derived from the ϵ^1 -order approximation. This mismatch leads to an energetic inconsistency. The present work resolves this issue by deriving both the elastodynamic equation and the damage/fracture law from the same ϵ^1 -order approximation of the strain and kinetic energy functions. Furthermore, in Appendix C, we verify that the proposed quasi-static and dynamic fracture models satisfy the Clausius–Duhem inequalities (C.1) and (C.5).

5. Numerical simulation

In this section, we present numerical simulations to illustrate the distinctive features and predictive capability of the proposed model. Although a large number of randomly oriented microcracks exist in real materials, under a given tensile stress state it is typically those perpendicular to the principal stress direction that would be preferentially activated, rather than all microcracks simultaneously be activated. Hence, under z-directional tension, we consider horizontal microcracks as the effective defects, as shown in Fig. 1.

We begin by establishing the relationships between the homogenized tensors $\hat{\mathbf{C}}, \hat{\mathbf{D}}, \hat{\mathbf{F}}$ and the damage variable S . Next, we perform local analyses, including both quasi-static and dynamic simulations. In particular, the strain rate dependent fracture strength is investigated and compared with experimental results. Additionally, the wave dispersion characteristics are investigated. Finally, finite element simulations are conducted to investigate structural responses, including tensile tests on plates with V-shaped notches and spalling fracture of a parallelepiped subjected to impact loading. The numerical results for spalling are compared with experimental data for validation.

For the numerical simulation, unless otherwise specified, the following material properties for titanium-aluminum alloy are used:

$$E = 2.1 \times 10^{11} \text{ Pa}, \quad \nu = 0.3, \quad \rho = 3890 \text{ kg/m}^3, \quad G_c = 2.7 \times 10^3 \text{ J/m}^2. \quad (34)$$

The Rayleigh wave velocity C_R is approximated by (Freund, 1990):

$$C_R \approx \frac{0.862 + 1.14\nu}{1 + \nu} \sqrt{\frac{E}{2\rho(1 + \nu)}}. \quad (35)$$

5.1. Relationship between $\hat{\mathbf{C}}, \hat{\mathbf{D}}, \hat{\mathbf{F}}$ and S

From the definitions of the effective tensors $\hat{\mathbf{C}}, \hat{\mathbf{D}}, \hat{\mathbf{F}}$ in Eqs. (14a), (14c), and (17c), each component is expressed as an integral involving the first-order cell functions \mathbf{N}^{pq} and the second-order cell functions \mathbf{N}^{pqr} over the unit cell Y , which contains a centrally located penny-shaped microcrack. Consequently, the components of these tensors depend explicitly on the damage variable S .

For each specified value of S , the cell problems given in Eqs. (9) and (10) are solved using the finite element method to obtain \mathbf{N}^{pq} and \mathbf{N}^{pqr} , respectively. The effective tensors $\hat{\mathbf{C}}(S), \hat{\mathbf{D}}(S)$, and $\hat{\mathbf{F}}(S)$ are then computed according to Eqs. (14a), (14c), and (17c). To determine their functional dependence on the damage variable, we evaluate these tensors over a discrete set of values $S = \{4\pi R^2 \mid R = 0, 0.0045, \dots, 0.4999\}$, and construct continuous functional representations using cubic spline interpolation.

For a penny-shaped crack, $\hat{\mathbf{C}}$ has 5 independent components (see Appendix B). The variation of the independent components \hat{C}_{ijkl} with S is shown in Fig. 3. All nonzero components of $\hat{\mathbf{C}}$ decrease with increasing S . \hat{C}_{3333} decreases significantly, while \hat{C}_{1111} decreases slowly, indicating a substantial reduction in stiffness perpendicular to the crack surface and less reduction parallel to it.

The homogenized strain gradient stiffness tensor $\hat{\mathbf{D}}$ contains 21 independent components, while the micro-inertia tensor $\hat{\mathbf{F}}$ contains 4 independent components (see Appendix B). Figs. 4 and 5 illustrate the variation of the nonzero components of $\hat{\mathbf{D}}$ and $\hat{\mathbf{F}}$ as functions of the damage variable S .

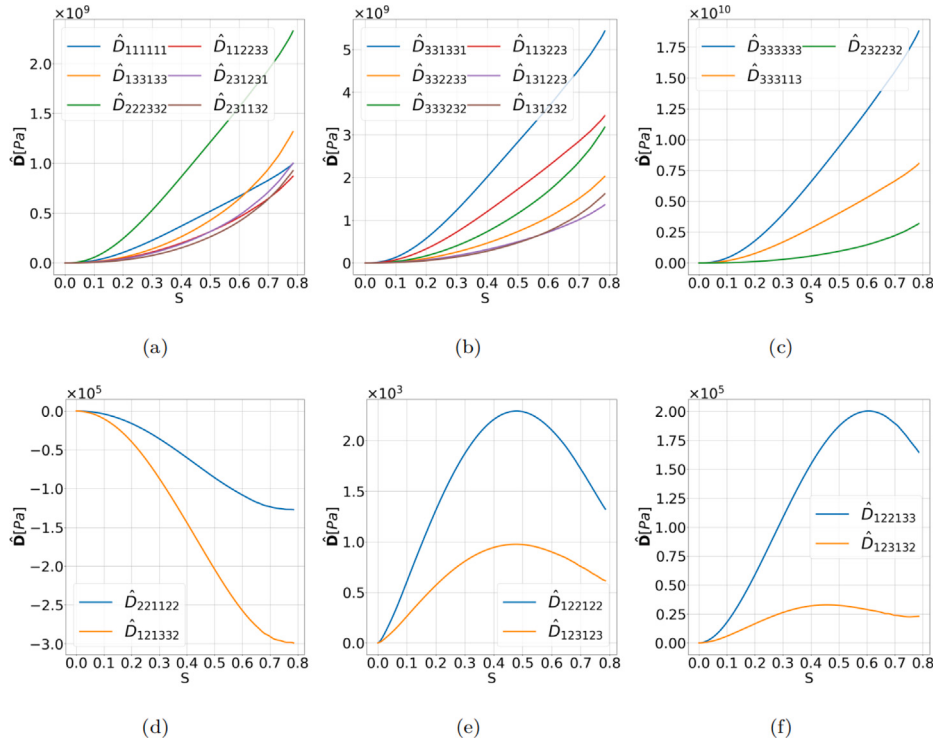


Fig. 4. Variation of the homogenized parameters \hat{D}_{ijklmn} with the damage variable S .

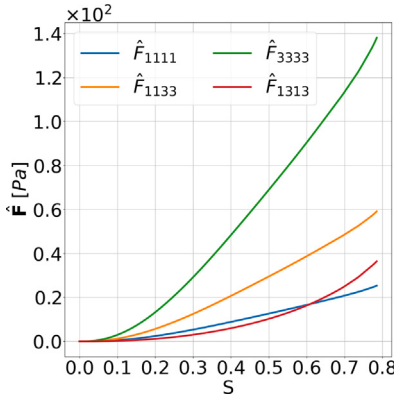


Fig. 5. Variation of the homogenized parameters \hat{F}_{ijkl} with the damage variable S .

For the undamaged material ($S = 0$), all components vanish, indicating that both strain gradient and strain rate effects can be neglected—consistent with classical strain gradient theory for homogeneous materials (Barboula and Li, 2018; Yang et al., 2022). As S increases from 0 to $\frac{\pi}{4}$, the dominant components of $\hat{\mathbf{D}}$ and $\hat{\mathbf{F}}$ exhibit monotonic growth, while several secondary components show non-monotonic behavior. This suggests that both strain gradient and strain rate effects become increasingly significant with the accumulation of damage.

Fig. 6 presents the eigenvalues of the effective moduli tensors $\hat{\mathbf{C}}$, $\hat{\mathbf{D}}$, $\hat{\mathbf{F}}$ in their Voigt matrix representations (see Figs. B.24–B.26), plotted as functions of the damage variable S . It is observed that all eigenvalues remain strictly positive throughout the evolution of S , thereby confirming the positive definiteness of the tensors. This property ensures the well-posedness of the governing equations Eqs. (27) and (28), as discussed in Remark 2.

Fig. 7 displays the eigenvalues of the derivatives $\frac{\partial \hat{\mathbf{C}}}{\partial S}$, $\frac{\partial \hat{\mathbf{D}}}{\partial S}$, and $\frac{\partial \hat{\mathbf{F}}}{\partial S}$, which represent the contributions of strain, strain gradient, and strain rate to the energy release rate respectively (Eq. (30)).

As shown in Fig. 7(a), all eigenvalues of $\frac{\partial \hat{\mathbf{C}}}{\partial S}$ are non-positive, indicating that this fourth-order tensor is negative semi-definite. This suggests that the energy release rate increases with increasing strain, thereby promoting microcrack growth. Furthermore, all eigenvalues of $\frac{\partial \hat{\mathbf{C}}}{\partial S}$ tend to decrease as the damage variable S increases, with the most pronounced decrease observed in the smallest eigenvalue. This implies that the second derivative of the energy release rate with respect to S , in the absence of strain gradient and strain rate effects, satisfies

$$-\frac{\partial^2}{\partial S^2} \{ \hat{C}_{ijkl}(S) \mathcal{E}_{ij} \mathcal{E}_{kl} \} \geq 0.$$

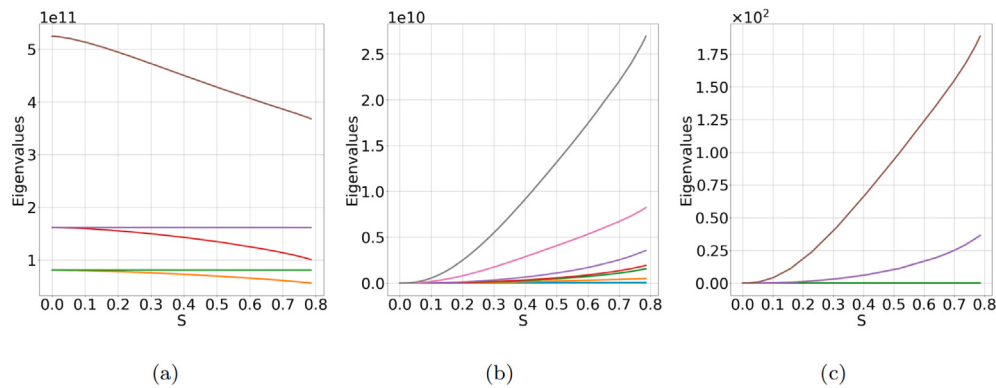


Fig. 6. Eigenvalues of $\hat{\mathbf{C}}$, $\hat{\mathbf{D}}$, and $\hat{\mathbf{F}}$ as functions of the damage variable parameter S .

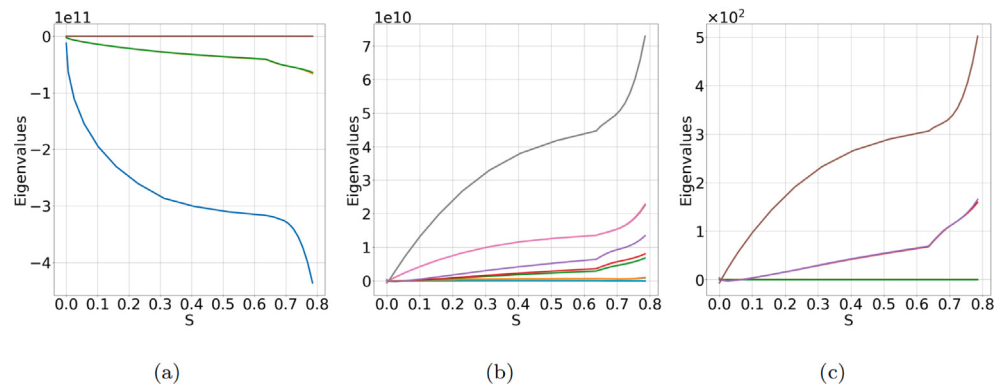


Fig. 7. Eigenvalues of $\frac{\partial \hat{\mathbf{C}}}{\partial S}$, $\frac{\partial \hat{\mathbf{D}}}{\partial S}$, and $\frac{\partial \hat{\mathbf{F}}}{\partial S}$ as functions of the damage variable S .

Such behavior indicates that, without introducing strain gradient and strain rate effects, microcrack propagation is intrinsically unstable. Once instability is initiated, cracks tend to rapidly propagate throughout the entire RVE.

In contrast, Figs. 7(b) and (c) show that the eigenvalues of $\frac{\partial \hat{\mathbf{D}}}{\partial S}$ and $\frac{\partial \hat{\mathbf{F}}}{\partial S}$ are non-negative, indicating that these tensors are positive semi-definite. This behavior implies that higher strain gradients or strain rates reduce the energy release rate and thereby inhibit the propagation of microcracks.

Based on the variations trend of $\hat{\mathbf{C}}$, $\hat{\mathbf{D}}$, and $\hat{\mathbf{F}}$, as well as their derivatives with respect to the normalized crack area S , we can further clarify the physical interpretation of the homogenized energy functions. The strain energy function (18), dominated by the contribution of strain, represents the capacity of the damaged RVE to store elastic energy, which progressively decreases as microcrack growth reduces the effective stiffness. Similarly, in the energy release rate (33), the strain contribution can be interpreted as a driving force for crack propagation, with an increase in strain promoting microcrack extension. In contrast, the strain-gradient terms capture the additional energetic cost associated with nonuniform deformation during microcrack growth, reflecting the microstructure's resistance to highly localized strain fields. Likewise, the strain-rate terms in the kinetic energy (19) and the energy release rate incorporate micro-inertia effects, accounting for the influence of heterogeneous microcrack motions on dynamic responses and thereby penalizing rapid temporal variations. Collectively, these contributions regulate the energy release rate: while the reduction of strain energy with increasing damage promotes crack extension, the positive semi-definiteness of the gradient and inertia terms provides a stabilizing effect by elevating the energetic barrier to fracture.

5.2. Single-element analyses

In this section, we present the local mechanical response of a material point at the macro-scale, which corresponds to the mechanical response of a Gaussian point in finite element simulations.

5.2.1. Microstructural size-strength relationship

We begin by analyzing the Hall-Petch relation to elucidate the role of microstructural features in governing fracture resistance. In this subsection, all components of the strain, strain gradient, and strain rate tensors are set to zero, except for ε_{33} , which is prescribed to simulate uniaxial tension perpendicular to the crack surface. This loading condition induces a quasi-static Mode-I fracture.

The relationships between the critical stress Σ_c and the RVE size (average microcrack spacing) ε , as well as its inverse square root $1/\sqrt{\varepsilon}$, for various initial damage levels S_0 , are depicted in Figs. 8(a) and 8(b), respectively. As shown in Fig. 8(a), for a fixed initial damage S_0 , the critical stress Σ_c decreases with increasing strain ε . Conversely, for a fixed ε , Σ_c decreases as S_0 increases. This behavior mainly results from material softening due to a larger initial damage variable S_0 .

It is also evident from Fig. 8(b) that the critical stress Σ_c exhibits an approximately linear dependence on $1/\sqrt{\varepsilon}$. This observation is consistent with the well-known Hall-Petch relation (Hall, 1951; Petch, 1953), which describes the inverse square-root dependence of strength on microstructural length scales.

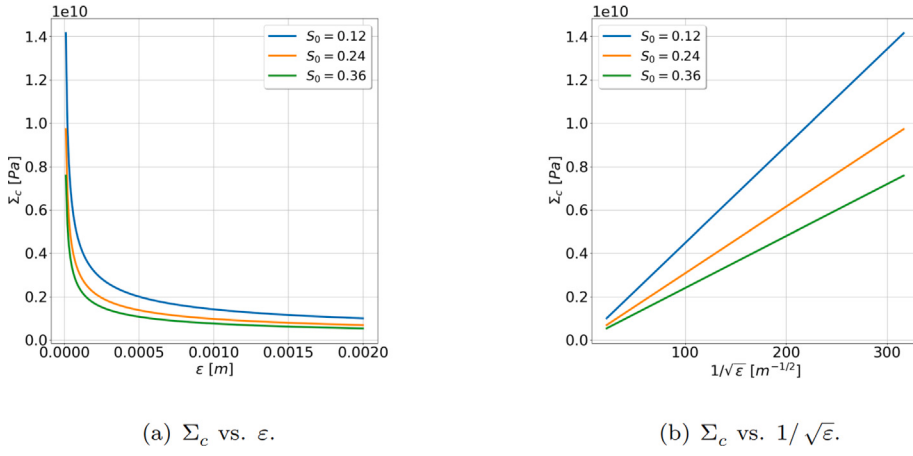


Fig. 8. Critical-stress as a function of ϵ or $1/\sqrt{\epsilon}$ for different S_0 .

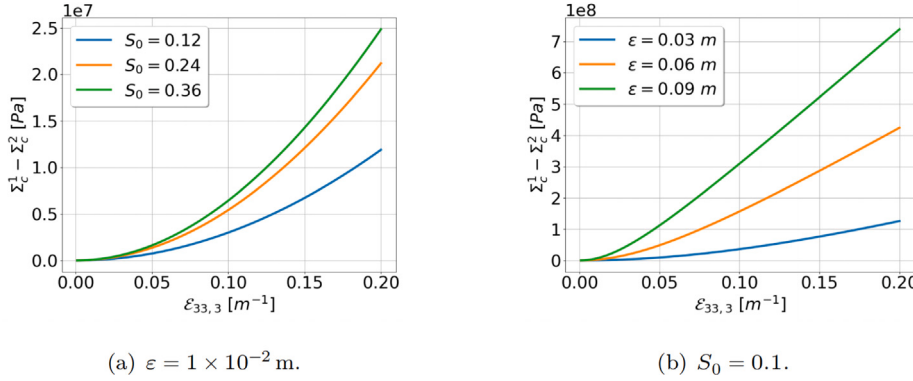


Fig. 9. Difference between the critical stress computed with and without the strain gradient term.

In fact, based on the quasi-static energy release rate given in Eq. (33) and the instability condition $G^{\text{static}} = G_c$, we can demonstrate that

$$\begin{aligned} \Sigma_c &= \hat{C}_{3333}\mathcal{E}_{33} = \epsilon^{-1/2}\hat{C}_{3333}\left[-\frac{\partial\hat{C}_{3333}(S)}{\partial S}\right]^{-1/2}\left[2G_c + \epsilon^3\frac{\partial\hat{D}_{333333}(S)}{\partial S}\mathcal{E}_{33,3}^2\right]^{1/2} \\ &\approx \sqrt{2G_c}\epsilon^{-1/2}\hat{C}_{3333}\left[-\frac{\partial\hat{C}_{3333}(S)}{\partial S}\right]^{-1/2} + \frac{\epsilon^{5/2}}{2\sqrt{2G_c}}\hat{C}_{3333}\left[-\frac{\partial\hat{C}_{3333}(S)}{\partial S}\right]^{-1/2}\frac{\partial\hat{D}_{333333}(S)}{\partial S}\mathcal{E}_{33,3}^2. \end{aligned} \quad (36)$$

When ϵ is sufficiently small, the effect of the strain gradient becomes negligible, and the above expression reduces to

$$\Sigma_c = \hat{C}_{3333}\mathcal{E}_{33} = \sqrt{2G_c}\hat{C}_{3333}\left[-\frac{\partial\hat{C}_{3333}(S)}{\partial S}\right]^{-1/2}\epsilon^{-1/2}, \quad (37)$$

which provides a clear physical interpretation of the parameters appearing in the Hall–Petch relationship.

5.2.2. Strain gradient effects

Next, we investigate the influence of the strain gradient on the critical stress. Specifically, when the strain gradient is included, the critical stress Σ_c is computed using Eq. (36), denoted as Σ_c^1 ; when the strain gradient is neglected, it is computed using Eq. (37), denoted as Σ_c^2 . Fig. 9 shows the variation of $\Sigma_c^1 - \Sigma_c^2$ with strain gradient $\mathcal{E}_{33,3}$ for various values of ϵ and S_0 .

From the figure, it is evident that the difference remains positive for any fixed combination of S_0 and ϵ , indicating that neglecting the strain gradient term leads to an underestimation of the material's fracture strength. This behavior originates from the positive definiteness of $\frac{\partial D(S)}{\partial S}$, as illustrated in Fig. 7(b), which contributes negatively to the energy release rate in Eq. (30). Consequently, the inclusion of the strain gradient term increases the energy barrier for crack propagation, thereby elevating the critical fracture stress.

Moreover, as shown in Fig. 9(a), the influence of the strain gradient effect becomes more pronounced as S_0 increases. This trend aligns with the increasing eigenvalues of $\frac{\partial D}{\partial S}$ with respect to S . Additionally, Fig. 9(b) illustrates that the difference between Σ_c^1 and Σ_c^2 grows with ϵ , suggesting that the strain gradient plays a more significant role at larger microstructural length scales. This outcome highlights the size-dependent strain gradient strengthening effect introduced by microstructural features, consistent with previously reported findings (Peerlings and Fleck, 2004; Li, 2011b; Li et al., 2011b).

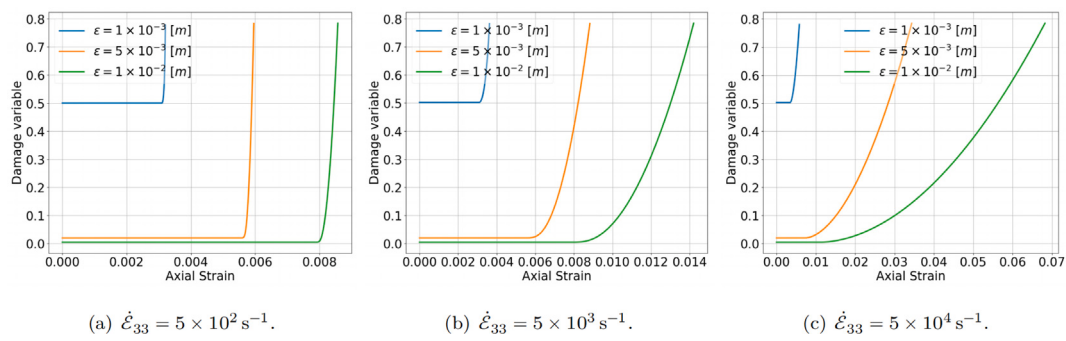
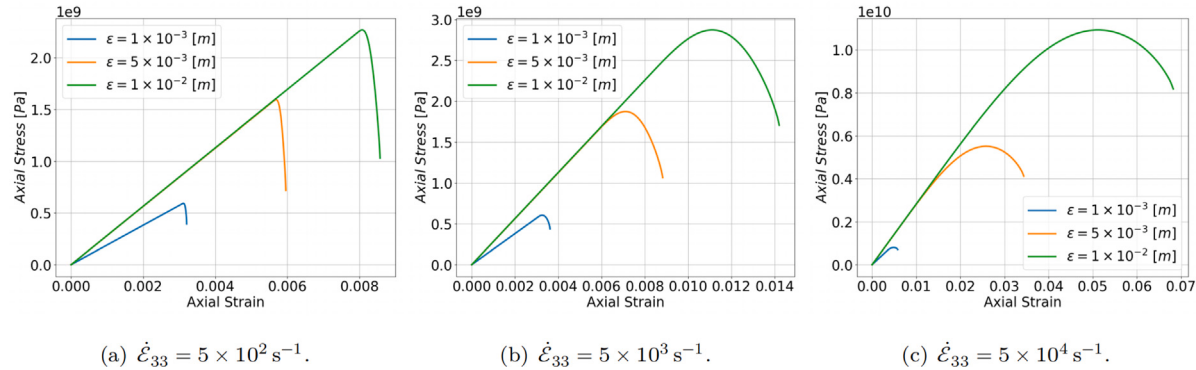
Fig. 10. Damage evolution curve with fixed $s_0 = 5 \times 10^{-7} \text{ m}^2$.Fig. 11. Constitutive relation with fixed $s_0 = 5 \times 10^{-7} \text{ m}^2$.

Table 1
Material properties used in rate-dependent tensile strength testing.

Material	E (Pa)	ν (-)	ρ (kg/m^3)	G_c (J/m^2)
Dry HB50 (Forquin and Erzar, 2009)	3.1×10^{10}	0.2	2200	10
Wet HB50 (Forquin and Erzar, 2009)	3.8×10^{10}	0.2	2320	15
R30A7 (Erzar and Forquin, 2011; Dascalu, 2024)	3.1×10^{10}	0.2	2200	60
Alumina ceramics (Zinszner et al., 2015; Dascalu, 2024)	3.6×10^{11}	0.22	3850	40

5.2.3. Strain rate effects

In this subsection, we investigate the influence of strain rate on the dynamic fracture process. We conduct uniaxial tension simulations on a representative macroscopic material point subjected to a constant strain rate. Except for \mathcal{E}_{33} and $\dot{\mathcal{E}}_{33}$, all other components of the strain and strain rate tensors are assumed to be zero, and strain gradient effects are neglected.

We first fix the initial microcrack area s_0 and vary the average spacing ϵ . In this case, decreasing ϵ leads to a higher density of microcracks and, consequently, a greater initial damage level, given by $S_0 = s_0/\epsilon^2$.

Fig. 10 illustrates the evolution of the damage variable S under different strain rate conditions. When the strain rate $\dot{\mathcal{E}}_{33}$ is held fixed, an increase in the initial microcrack density renders the material more susceptible to complete failure. On the other hand, when ϵ is fixed, the damage evolution exhibits distinct behaviors under varying strain rates. At relatively low strain rates – e.g., $\dot{\mathcal{E}}_{33} = 5 \times 10^2 \text{ s}^{-1}$ in Fig. 10(a) – material instability is accompanied by a sharp rise in the damage variable, indicating a fracture response closer to brittle failure. As the strain rate increases (see Figs. 10(b), (c)), microcrack growth becomes more gradual, signifying a transition toward ductile behavior.

Fig. 11 shows the stress–strain relations $\Sigma_{33}(\mathcal{E}_{33}) = \hat{C}_{3333}(\mathcal{S}(\mathcal{E}_{33})) \cdot \mathcal{E}_{33}$. It is observed that for a given strain rate $\dot{\mathcal{E}}_{33}$ and average spacing ϵ , the stress increases linearly with strain until the onset of damage. Once damage initiates, the stress continues to rise momentarily, followed by a rapid drop. For a fixed strain rate, decreasing ϵ – which corresponds to increasing microcrack density – leads to material softening and a reduction in peak stress. With a fixed ϵ , increasing the strain rate results in a smoother stress drop and a less abrupt failure, further confirming that the material response transitions from brittle to ductile with increasing strain rate.

Fig. 12 provides further insight into the role of strain rate in dynamic fracture. As the strain rate increases, the material response gradually transitions from brittle to ductile, as evidenced by the smoother evolution of the damage variable and the less abrupt stress drop. Furthermore, a higher strain rate delays the onset of instability and leads to an increase in the maximum stress that the material can sustain, indicating a rate-dependent strengthening effect. These results collectively suggest that micro-inertia contributes to the suppression of damage accumulation and enhances the material's fracture resistance, which is consistent with experimental findings reported in Erzar and Forquin (2010), Zinszner et al. (2015).

Fig. 13 presents a comparison between the predicted and experimental values of tensile strength as a function of strain rate for the material listed in Table 1. Fig. 13(a) and (b) depict the tensile strength of dry and wet HB50, respectively, with an initial damage level of $S_0 = 0.2$. The predicted tensile strength is compared with experimental data from Toutlemonde (1994), Cadoni et al. (2001), Forquin and Erzar (2009). For

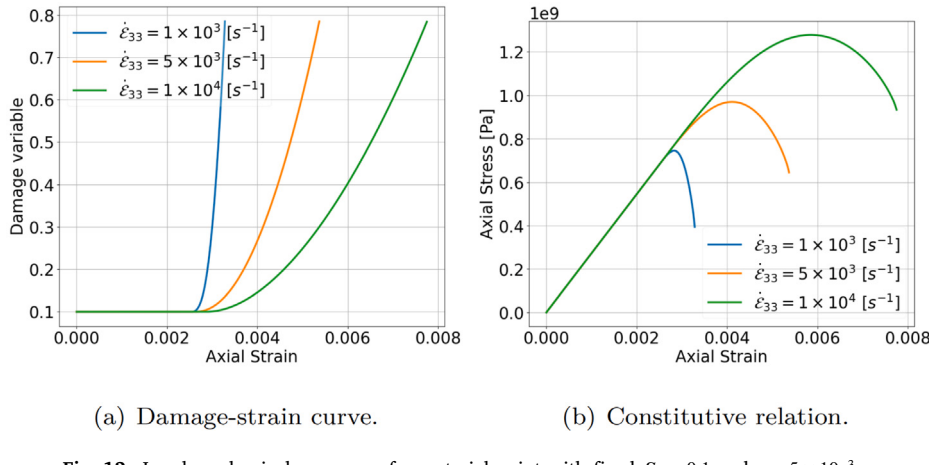


Fig. 12. Local mechanical response of a material point with fixed $S_0 = 0.1$ and $\varepsilon = 5 \times 10^{-3}$ m.

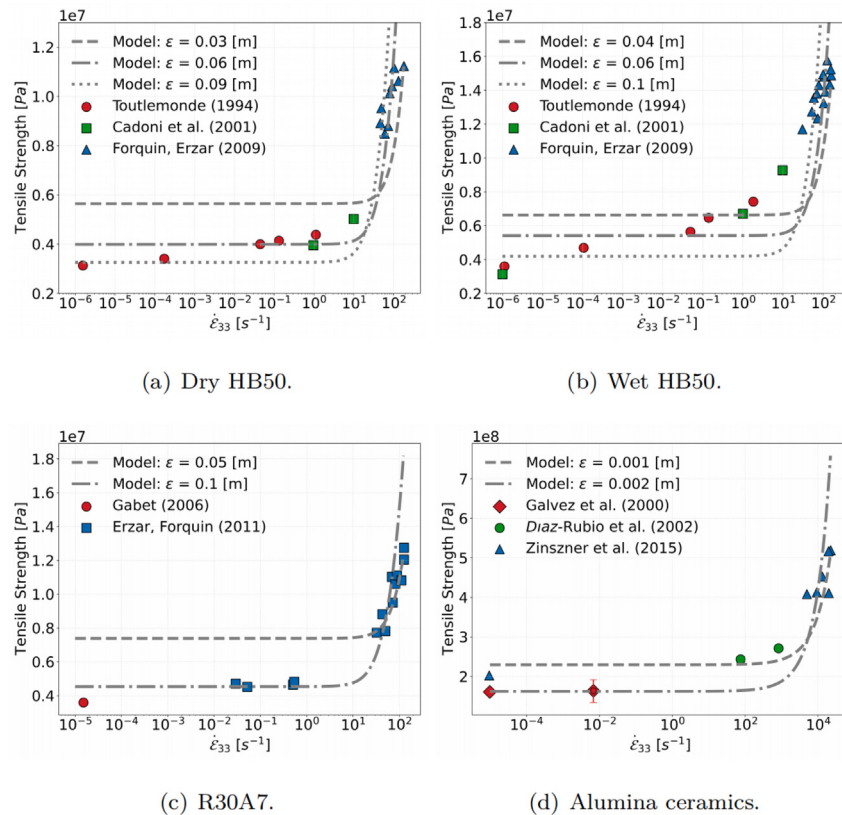


Fig. 13. Tensile strength: model predictions and experimental data.

the R30A7 standard concrete in the third experiment (Fig. 13(c)), the initial damage level is set to $S_0 = 0.5$, with experimental data from Gabet (2006), Erzar and Forquin (2011). The fourth experiment, shown in Fig. 13(d), examines high-purity alumina (99.7 %) with an initial damage level of $S_0 = 0.15$, using experimental data from Gálvez et al. (2000), Diaz-Rubio et al. (2002), Zinszner et al. (2015).

Fig. 13 shows good agreement between the predicted and experimental tensile strengths, demonstrating the model's predictive accuracy. It also indicates that a larger ε yields better predictions at lower strain rates, whereas a smaller ε is more suitable at higher strain rates. This behavior can be attributed to the increased instability of the material as the strain rate rises, which leads to the activation of more microcracks. Consequently, the characteristic length scale – representing the average fragment size or the spacing between activated microcracks – decreases (Zhou et al., 2006; Li et al., 2018; Dascalu, 2024). Therefore, a smaller value of ε is necessary to accurately capture the fracture process at higher strain rates. This reinterpretation suggests that ε corresponds to the spacing between dynamically activated cracks, rather than being an intrinsic material property.

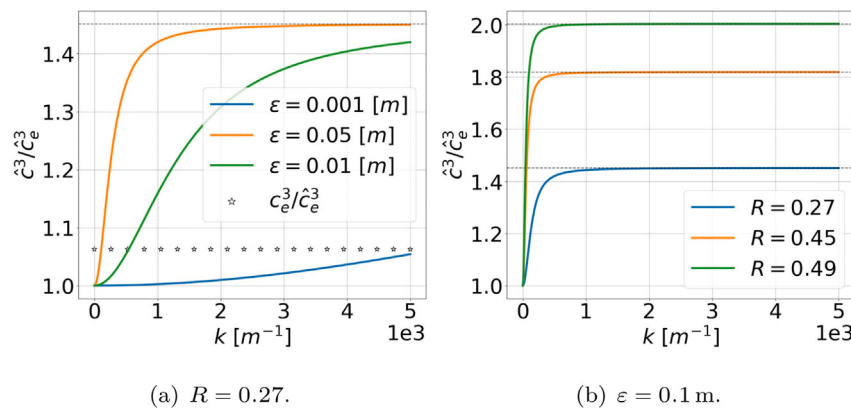


Fig. 14. Normalized phase velocity \hat{c}^3/\hat{c}_e^3 v.s. wave number k .

5.3. One-dimensional analyses - wave dispersion

Wave propagation in microstructured materials, such as damaged solids, differs significantly from that in ideal, defect-free media, often exhibiting dispersive behavior (Gross and Zhang, 1992; Keita et al., 2014; Berezovski et al., 2020). The framework of strain gradient elastodynamics provides an effective means of capturing such dispersion phenomena in microstructured continua.

Consider a material containing microcracks periodically spaced by ε with normalized crack radius R . The propagation of a one-dimensional longitudinal (P-) wave, represented by the displacement component $u_3(x_3, t)$ along the direction perpendicular to the crack faces, satisfies the following partial differential equation:

$$\hat{C}_{3333} \frac{\partial^2 u_3}{\partial x_2^2} - \epsilon^2 \hat{D}_{333333} \frac{\partial^4 u_3}{\partial x_2^4} = \hat{\rho} \ddot{u}_3 - \epsilon^2 \hat{F}_{3333} \frac{\partial^2 \dot{u}_3}{\partial x_2^2}. \quad (38)$$

To derive the dispersion relation, we assume a harmonic wave solution of the form:

(39)

$$u_3(x_3, t) = \hat{u}_3 e^{i(kx_3 - \omega t)},$$

where k is the wavenumber, ω is the angular frequency, and i is the imaginary unit ($i^2 = -1$).

Substituting Eq. (39) into Eq. (38) yields the following dispersion relation for the phase velocity:

$$\hat{e}^{(3)} = \frac{\omega}{k} = \sqrt{\frac{\hat{C}_{3333} + k^2 \epsilon^2 \hat{D}_{333333}}{\hat{\rho} + k^2 \epsilon^2 \hat{F}_{3333}}} = \hat{e}_e^3 \sqrt{\frac{1 + \frac{k^2 \epsilon^2 \hat{D}_{333333}}{\hat{C}_{3333}}}{1 + \frac{k^2 \epsilon^2 \hat{F}_{3333}}{\hat{\rho}}}}, \quad (40)$$

where $\hat{c}_e^3 = \sqrt{\hat{C}_{3333}/\hat{\rho}}$ denotes the phase velocity predicted by the classical homogenized elastic model (i.e., Eq. (28) without strain gradient term and strain rate term), which is constant and independent of the wavenumber.

Fig. 14 presents the dispersion curves computed for various values of the microstructural parameters ϵ and R . As shown in the figure, when $k \rightarrow 0$, the phase velocity \hat{c}^3 approaches the homogenized value c_e^3 . This behavior indicates that when the wavelength of the incident wave is much larger than the characteristic microstructural length scale, the material effectively behaves as a homogeneous medium, and the strain gradient and strain rate effects become negligible. Due to the presence of microcracks, the effective stiffness tensor $\hat{\mathbf{C}}$ is reduced compared to the undamaged case, while the effective mass density $\hat{\rho}$ remains approximately unchanged. Consequently, the phase velocity in the damaged (microcracked) material is lower than that in the undamaged medium, i.e., $\hat{c}^3 < c_e^3$. Here, $c_e^3 = \sqrt{C_{3333}/\rho}$ denotes the phase velocity in a homogeneous material without microcracks.

As the wavelength decreases and becomes comparable to the microcrack spacing or size, nonlocal interactions become increasingly significant. In this short-wavelength regime, the microstructure induces localized scattering and potential resonance effects. As $k \rightarrow \infty$, the normalized phase velocity asymptotically approaches a finite limit:

$$\lim_{k \rightarrow \infty} \frac{c^{(3)}}{c_{\text{min}}^{(3)}} = \sqrt{\frac{\hat{D}_{3333333}/\hat{C}_{33333}}{\hat{F}_{33333}/\hat{\rho}}}.$$

It is important to note that neglecting the strain rate term in the elastodynamic equation (Eq. (27)), specifically the term involving \hat{F}_{3333} , leads to a divergence of the phase velocity as $k \rightarrow \infty$. This results in an unphysical prediction of infinite wave speed at vanishing wavelengths.

Furthermore, the degree of wave dispersion is significantly enhanced by increasing either the microstructural length scale ϵ or the damage level, underscoring the pronounced influence of microstructural features on the dynamic response of the material.

We note that Keita et al. (2014) derived a dispersion relation for two-dimensional solids containing microcracks. However, their formulation relies on several assumptions, including quadratic dependence of the elastic moduli on the damage variable, the same frequency and wave number for displacement and damage field, as well as linearized forms of both the damage evolution law and the elastodynamic equation. In the formulation of Keita et al. (2014), dispersive effects arise from the evolution of damage and vanish in the absence of damage growth. The present work establishes the dispersion relation without resorting to such additional assumptions, thereby providing a more general and rigorous theoretical framework. The present model can capture dispersion induced purely by the presence of microcracks, even when no further propagation of micro-cracks occurs. Our result shows that phase velocity increases as wave number increases, qualitatively consistent with that reported by Keita et al. (2014).

5.4. Three-dimensional structural analyses

In this subsection, we further investigate the influence of strain gradient and strain rate on macroscopic brittle fracture through two representative cases: the tensile fracture of a V-notched plate and the spalling fracture of a parallelepiped.

As described in Section 5.1, the material coefficients are expressed as functions of the damage variable through spline interpolation, denoted by $\hat{C}_{ijkl}(S)$, $\hat{D}_{ijklmn}(S)$, and $\hat{F}_{ijkl}(S)$.

In the numerical simulations of macroscopic dynamic fracture, a staggered strategy is adopted to update the displacement field \mathbf{u} and the damage field S . The time domain is discretized into increments of size Δt , with $t_n = n\Delta t$. At each time step $[t_n, t_{n+1}]$, the damage field is first held fixed. The displacement and velocity fields are updated using the finite element method with a tetrahedral mesh for spatial discretization, combined with the leap-frog scheme for temporal integration. Subsequently, with the displacement and velocity fields fixed, the energy release rate is computed according to Eq. (27), followed by the update of the damage field through Eq. (32). The staggered procedure is summarized in Algorithm 1.

The displacement field is discretized using P_2 elements, with the C^0 interior penalty method applied to enforce gradient continuity (Brenner and Neilan, 2011), while the damage field is discretized using P_0 elements. The mass matrix \mathbf{M} , stiffness matrix \mathbf{K} , and external force vector $\mathbf{F}(t)$ are defined as

$$\begin{aligned} M_{pq} &= \int_{\Omega} \hat{\rho} \Phi_p(\mathbf{x}) \Phi_q(\mathbf{x}) \, d\mathbf{x} + \varepsilon^2 \int_{\Omega} \hat{F}_{ijkl} e_{ij}(\Phi_p)(\mathbf{x}) e_{kl}(\Phi_q)(\mathbf{x}) \, d\mathbf{x}, \\ K_{pq} &= \int_{\Omega} \hat{C}_{ijkl} e_{ij}(\Phi_p(\mathbf{x})) e_{kl}(\Phi_q(\mathbf{x})) \, d\mathbf{x} + \varepsilon^2 \int_{\Omega} \hat{D}_{ijklmn} e_{ijk}(\Phi_p)(\mathbf{x}) e_{lmn}(\Phi_q)(\mathbf{x}) \, d\mathbf{x}, \\ F_p(t) &= \int_{\Omega} f(t, \mathbf{x}) \Phi_p(\mathbf{x}) \, d\mathbf{x}, \end{aligned}$$

where Φ_p denotes the finite element basis functions.

Algorithm 1: Staggered algorithm at time interval $[t_n, t_{n+1}]$

Input: damage field S_n , displacement field \mathbf{u}_n , and velocity field $\dot{\mathbf{u}}_{n+1/2}$ at previous time step t_n .
Output: damage field S_{n+1} , displacement field \mathbf{u}_{n+1} , and velocity field $\dot{\mathbf{u}}_{n+3/2}$ at current time step t_{n+1} .

- 1 Set $i = 0$, tolerance $= 1 \times 10^{-8}$;
- 2 Initialize $S_{n+1}^{(0)} \leftarrow S_n$, $\mathbf{u}_{n+1}^{(0)} \leftarrow \mathbf{u}_n$, $\dot{\mathbf{u}}_{n+1}^{(0)} \leftarrow \dot{\mathbf{u}}_n$;
- 3 **repeat**
- 4 Update material coefficients $\hat{C}_{ijkl}(S_{n+1}^{(i)})$, $\hat{D}_{ijklmn}(S_{n+1}^{(i)})$, $\hat{F}_{ijkl}(S_{n+1}^{(i)})$ and matrices \mathbf{M} , \mathbf{K} ;
- 5 $\mathbf{u}_{n+1}^{(i+1)} = \mathbf{u}_n^{(i)} + \Delta t \dot{\mathbf{u}}_{n+1/2}^{(i)}$;
- 6 $\dot{\mathbf{u}}_{n+1}^{(i+1)} = \mathbf{M}^{-1} (\mathbf{F}(t_{n+1}) - \mathbf{K} \mathbf{u}_{n+1}^{(i+1)})$;
- 7 $\dot{\mathbf{u}}_{n+1}^{(i+1)} = \dot{\mathbf{u}}_{n+1/2}^{(i+1)} + \frac{\Delta t}{2} \ddot{\mathbf{u}}_{n+1}^{(i+1)}$, $\mathbf{u}_{n+3/2}^{(i+1)} = \mathbf{u}_{n+1}^{(i+1)} + \frac{\Delta t}{2} \dot{\mathbf{u}}_{n+1}^{(i+1)}$;
- 8 Compute $S_{n+1}^{(i+1)}$ with fixed $\mathbf{u}_{n+1}^{(i+1)}$, $\dot{\mathbf{u}}_{n+1}^{(i+1)}$ by solving Eq. (32);
- 9 subject to the irreversibility constraint $S_n \leq S_{n+1}^{(i+1)} \leq \frac{\pi}{4}$;
- 10 $i \leftarrow i + 1$;
- 11 **until** $\|\mathbf{u}_{n+1}^{(i+1)} - \mathbf{u}_{n+1}^{(i)}\| + \|S_{n+1}^{(i+1)} - S_{n+1}^{(i)}\| \leq \text{tolerance}$;
- 12 Update solutions $S_{n+1} \leftarrow S_{n+1}^{(i)}$, $\mathbf{u}_{n+1} \leftarrow \mathbf{u}_{n+1}^{(i)}$, and $\dot{\mathbf{u}}_{n+1} \leftarrow \dot{\mathbf{u}}_{n+1}^{(i)}$;

For the quasi-static brittle fracture, the update of the displacement field is performed by solving Eq. (28), while the energy release rate is evaluated using Eq. (33). Once the computed energy release rate exceeds the critical fracture toughness G_c at location \mathbf{x} , the damage field is updated to the fully fractured state, i.e., $S = \frac{\pi}{4}$.

5.4.1. Tensile fracture of a V-notched plate

Firstly, we examine the influence of strain gradient effects on quasi-static tensile fracture, with particular emphasis on their impact on the predicted onset time of crack propagation. The geometry of the V-notched plate considered in the simulation is shown in Fig. 15. The constitutive constants are chosen according to Eq. (34). The plate is subjected to quasi-static loading applied on its upper and lower surfaces. At each loading step, a displacement increment of $\Delta u = [0, 0, 5 \times 10^{-7} \text{ m}]$ is imposed. The initial damage variable is prescribed as $S_0 = 0.1$. Exploiting the symmetry of the geometry with respect to the central axis, a symmetric mesh is employed for the plate. The mesh is further refined to $h = 0.18 \text{ mm}$ at the V-notch tip and in the potential crack propagation region.

In this simulation, we define a Griffith-type fracture criterion function as

$$\mathcal{G}(\mathbf{u}, S) = \frac{G_c}{G^{\text{static}}} = -G_c \left\{ \frac{\varepsilon}{2} \frac{\partial \hat{C}_{ijkl}(S)}{\partial S} \mathcal{E}_{ij} \mathcal{E}_{kl} + \frac{\varepsilon^3}{2} \frac{\partial \hat{D}_{ijklmn}(S)}{\partial S} \mathcal{E}_{ij,k} \mathcal{E}_{lm,n} \right\}^{-1}, \quad (41)$$

where \mathcal{E}_{ij} and $\mathcal{E}_{ij,k}$ denote the strain and strain gradient components, respectively.

When the condition $\mathcal{G}(\mathbf{u}, S; \mathbf{x}) \leq 1$ is satisfied at a given spatial location \mathbf{x} , the damage variable at that location is driven to its fully damaged state, i.e., $S = \frac{\pi}{4}$.

It is important to note that both the equilibrium equation (Eq. (28)) and the fracture criterion function (Eq. (41)) incorporate strain gradient-related terms. To systematically evaluate the individual and combined effects of strain gradient contributions, we consider four model variants by selectively including or excluding the gradient terms, as summarized in Table 2.

Fig. 16 shows the variation of the criterion function \mathcal{G} at the center of the V-notch tip with increasing applied displacement Δu . When $\varepsilon = 0.001 \text{ m}$, as illustrated in Fig. 16(a), retaining or omitting the strain gradient terms in either the governing equation or the fracture criterion yields similar results, indicating that the strain gradient effects are negligible when the microstructural length scale is small.

However, when ε increases to a value comparable to the macroscopic characteristic length (e.g., $\varepsilon = 0.005 \text{ m}$), the strain gradient effects become significantly more pronounced, as shown in Fig. 16(b). In this case, the onset of crack instability follows the order: Model 4 < Model 3 < Model 2

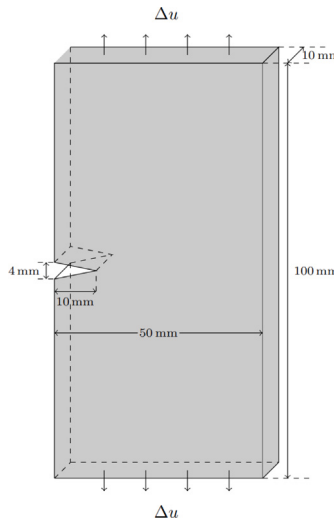


Fig. 15. Geometric configuration and boundary conditions for tensile fracture.

Table 2
Model configurations for assessing strain gradient effects.

Model	Strain gradient in equilibrium equation	Strain gradient in fracture criterion function
Model 1	true	true
Model 2	false	true
Model 3	true	false
Model 4	false	false

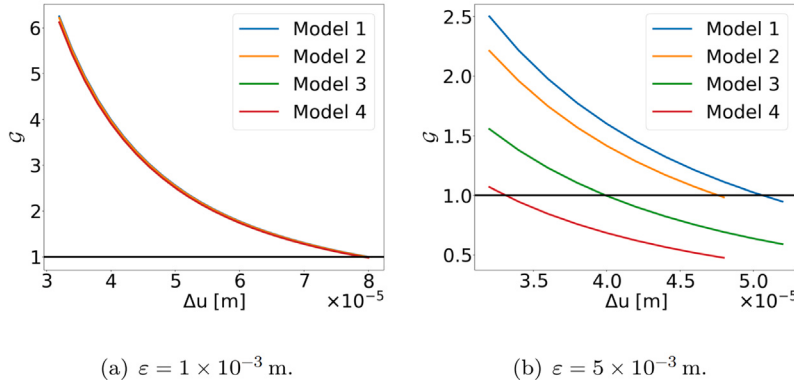


Fig. 16. Variation of the Griffith criterion function at the center of V-notch tip with Δu .

< Model 1. This trend is also evident in Fig. 17, where the spatial distribution of $1/G$ provides a clear visual comparison across different models. Comparing Model 1 with Model 3, or Model 2 with Model 4, indicates that omitting the strain gradient terms in the damage law leads to an underestimation of the fracture strength. The influence of the strain gradient on the damage law is primarily reflected in the energy release rate expression, Eq. (33). Due to the negative definiteness of $-\frac{\partial \mathbf{B}}{\partial S}$, incorporating the strain gradient term reduces the energy release rate.

The comparison between Model 3 and Model 4 further highlights that the inclusion of strain gradient terms in the equilibrium equation smooths the strain field and eliminates the stress singularities inherent in classical continuum theory (Askes and Aifantis, 2011; Hosseini and Niiranen, 2022). In the absence of this term, the computed strain field exhibits singular behavior, which, given the positive definiteness of $-\frac{\partial \mathbf{B}}{\partial S}$, leads to an overestimation of the energy release rate and thus an underestimation of the fracture strength.

When ϵ is further increased to 0.01 m (see Fig. 18), the role of the strain gradient term in the equilibrium equation becomes even more significant. As shown in the results from the dual strain gradient model (Model 1), the notch tip gradually becomes unstable under increasing external loads. In contrast, when using Model 2, the notch tip remains stable throughout the loading process, which is unphysical. This discrepancy arises because, in the absence of the strain gradient term in equilibrium equation, the computed strain field near the V-notch tip exhibits excessive singularity. As a result, the corresponding strain gradients become unrealistically large, leading to an overestimated resistance to crack growth. Consequently, the material at the V-notch tip fails to reach the instability condition, and fracture cannot initiate.

5.4.2. Spalling fracture of a parallelepiped

In this subsection, we present numerical simulations of shockless spalling fracture in alumina ceramics and compare the results with the experimental measurements reported by Zinszner et al. (2015). A parallelepiped specimen with dimensions 10 mm × 2.5 mm × 2.5 mm is modeled, as

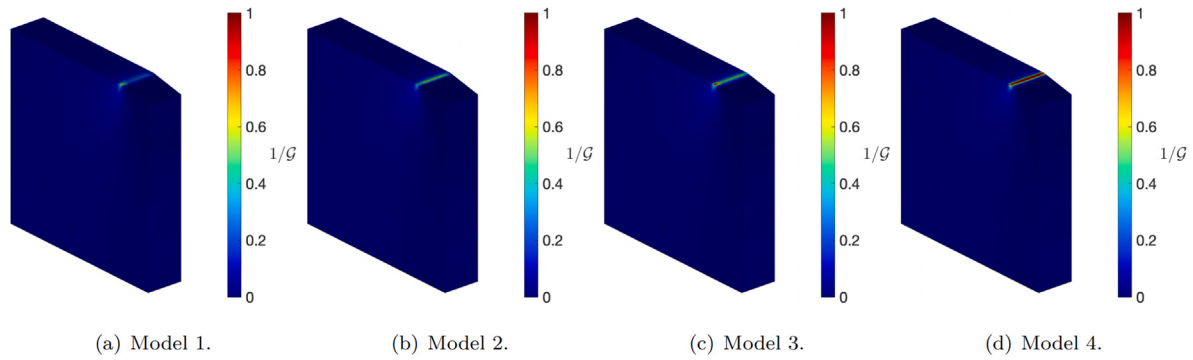


Fig. 17. Illustration of $1/\mathcal{G}$, with $S_0 = 0.1$, $\varepsilon = 5 \times 10^{-3}$ m, and $\Delta u = 3.8 \times 10^{-5}$ m.

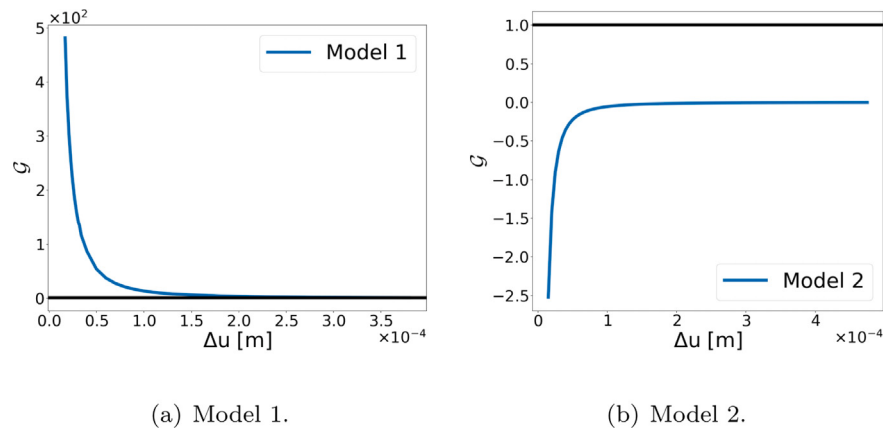


Fig. 18. Variation of the Griffith criterion function at the center of the V-notch tip with Δu for fixed $\varepsilon = 0.01$ m.

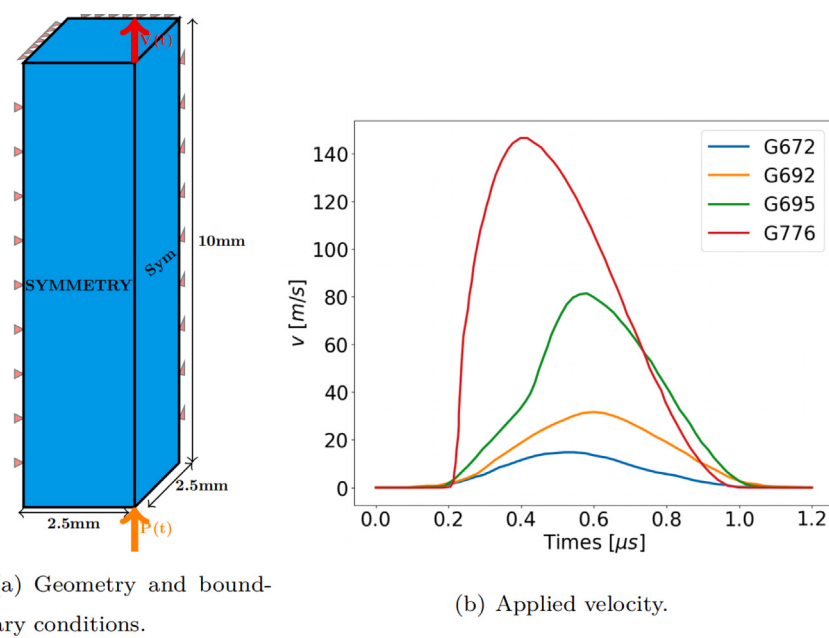


Fig. 19. Shockless spalling tests.

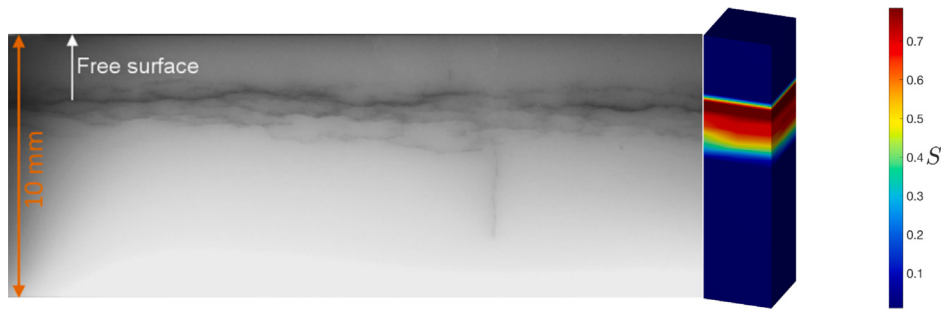


Fig. 20. Comparison of fracture zones between the experimental results reported in Zinszner et al. (2015) and the present numerical simulations for the G672 spalling test, with $S_0 = 0.01$ and $\varepsilon = 1 \text{ mm}$.

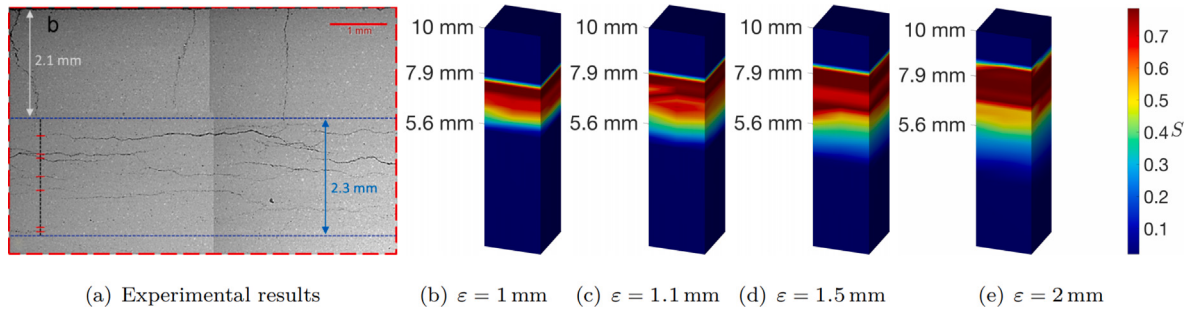


Fig. 21. Comparison of fracture zones between the experimental results in Zinszner et al. (2015) and the present numerical simulations with $S_0 = 0.01$ and varying ε , in the case of the G672 spalling test.

illustrated in Fig. 19(a). The material, AL23 alumina, is characterized by the following properties:

$$E = 3.6 \times 10^{11} \text{ Pa}, \quad \nu = 0.22, \quad \rho = 3890 \text{ kg/m}^3, \quad G_c = 50.752 \text{ J/m}^2.$$

In the experiment, a high-pulsed power generator is used to generate a compressive stress wave in the target. Upon reflection at the free surface, the compressive wave is transformed into rarefaction waves. The superposition of these rarefaction waves produces a region of tensile stress. If the tensile stress exceeds the material's fracture strength, spall failure occurs within the interior of the target plate (Antoun et al., 2003).

Four distinct velocity-time profiles, corresponding to the experimental loading conditions reported by Zinszner et al. (2015), are applied as boundary conditions on the lower face, as illustrated in Fig. 19(b). To maintain consistency with the experimental setup, symmetry boundary conditions are imposed on the internal faces of the specimen, while zero radial displacement boundary conditions ($U_r = 0$) are applied on the four lateral sides of the parallelepiped. The upper face is traction-free. The free-surface velocity is computed as the average over multiple nodes on the upper face to enhance robustness when comparing with experimental measurements, as shown in Fig. 19(a). A mesh size of 0.31 mm in the z -direction and a time step of $1 \times 10^{-9} \text{ s}$ are adopted to ensure both the accuracy and stability of the simulation.

Figs. 20 and 21 compare the fracture zones obtained from the present numerical simulations with the experimental observations reported by Zinszner et al. (2015) for the G672 spalling test. Overall, good agreement is achieved between the simulated and experimental fracture patterns. In particular, when $S_0 = 0.01$ and $\varepsilon = 1 \times 10^{-3} \text{ m}$, the predicted damaged zone initiates approximately 2.1 mm beneath the free surface, with a thickness of about 2.3 mm, which is in quantitative agreement with the experimental measurements.

On the other hand, as shown in Fig. 21, when the initial damage variable S_0 is fixed, the size of the fracture zone increases with increasing ε . This behavior can be explained by the relation $s_0 = \varepsilon^2 S_0$. For a fixed S_0 , a larger ε corresponds to a larger initial microcrack size, thereby facilitating more extensive damage evolution.

Fig. 22 shows the numerically predicted fracture zones under four different stress wave loadings, with a fixed initial damage parameter $S_0 = 0.1$ and a microstructural length scale $\varepsilon = 1 \text{ mm}$. It is observed that the size of the damaged zone is strongly dependent on the strain rate. As the strain rate increases, the damage zone progressively expands; specifically, the damaged region becomes denser and extends farther into the material. This observation is consistent with the results reported by Zinszner et al. (2015).

In spallation experiments, certain physical quantities – such as internal pressure and damage – are challenging to measure directly. Among the various measurable parameters, the free-surface velocity profile is one of the most commonly recorded. From this velocity signal, dynamic material properties – such as the Hugoniot elastic limit and the spall strength – can be inferred.

Fig. 23 shows the predicted free-surface velocity profiles under four different stress wave loadings, along with corresponding experimental data for comparison. Due to the limited availability of experimental data for the AL23 alumina specimen – particularly regarding the initial damage parameter S_0 and the microstructural length scale ε – these parameters are calibrated to achieve good agreement with the measured velocity profiles. In all simulations, the microstructural length scale is fixed at $\varepsilon = 1 \text{ mm}$, while the initial damage parameter S_0 is set to 0.1, 0.1, 0.2, and 0.3 for the G672, G692, G695, and G776 tests, respectively.

As shown in the figure, the numerical results closely match the experimental measurements, particularly in terms of the pull-back velocity, defined as the difference between the peak free-surface velocity and the velocity at the first rebound, which is associated with the spall strength. Minor discrepancies may arise from uncertainties in the selected microstructural parameters S_0 and ε , as well as from inherent limitations in experimental diagnostics. Additionally, thermal effects during the fracture process – neglected in the present model – may influence early-stage damage evolution, thereby contributing to the observed deviations.

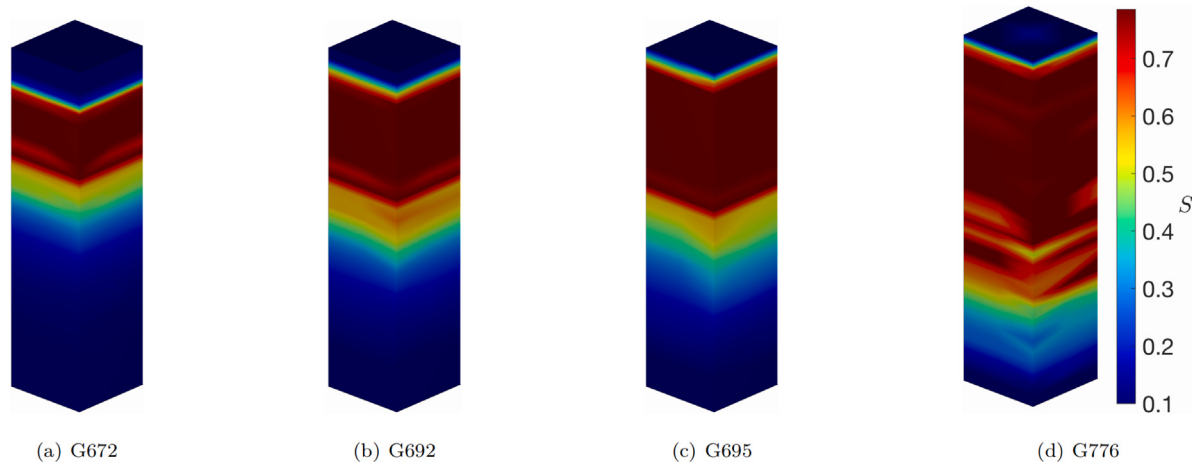


Fig. 22. Fracture zones obtained by applying different stress waves, with $S_0 = 0.1$ and $\varepsilon = 1 \text{ mm}$.

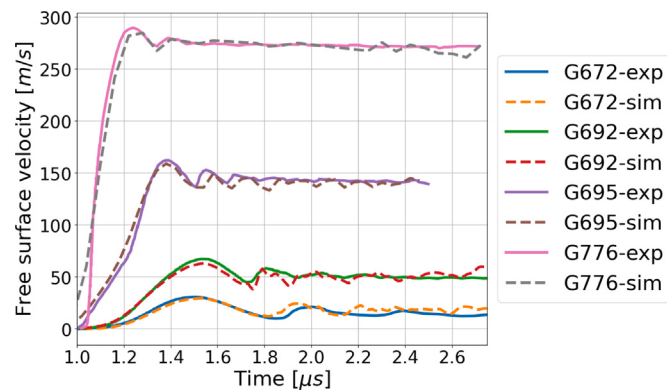


Fig. 23. Comparisons between experimental and numerical results for free surface velocity profiles.

6. Conclusion

In this work, we have developed an energetically consistent two-scale asymptotic framework for modeling the dynamic deformation and fracture of brittle materials. Both the strain-gradient elastodynamic equation and the damage/fracture evolution law are derived from the same ϵ^1 -order approximation of the homogenized strain and kinetic energy functions, thereby eliminating the energetic inconsistency inherent in previous formulations. A concise set of effective coefficients, expressed as integrals of cell functions depending only on intrinsic material parameters such as elastic moduli, microcrack size, and spacing, establishes a rigorous micromechanical linkage between the microscopic crack network and macroscopic fracture responses.

The predictive capability of the proposed model has been systematically evaluated through a hierarchy of numerical investigations.

At the material-point level, the framework provides a clear interpretation of the Hall-Petch relation, demonstrating the inverse square-root dependence of fracture strength on microstructural size. It further reveals that strain-gradient and strain-rate effects act as stabilizing mechanisms, increasing the critical stress for fracture and suppressing the instability of microcrack growth.

In one-dimensional analysis, dispersion studies show that the size and average spacing of microcracks influence wave dispersion. They also highlight the necessity of including strain-rate contributions in the elastodynamic equations, as neglecting them leads to non-physical artifacts, i.e., unbounded wave speeds at short wavelengths.

At the structural scale, simulations of notched specimens emphasize the importance of incorporating strain-gradient contributions in the elastic governing equations, since neglecting them results in stress singularities and an exaggerated inhibition of crack propagation due to strain-gradient effects. Spalling failure simulations under impact loading confirm that the model accurately predicts crack initiation, damage-zone morphology, and free-surface velocity profiles, in close quantitative agreement with experimental observations.

CRediT authorship contribution statement

Quanzhang Li: Writing – original draft, Visualization, Methodology, Investigation, Formal analysis. **Yipeng Rao:** Writing – review & editing, Validation, Formal analysis. **Xia Tian:** Writing – review & editing, Validation. **Jun Chen:** Writing – review & editing, Validation. **Xin Yu:** Writing – review & editing, Validation. **Junzhi Cui:** Writing – review & editing, Supervision, Conceptualization. **Meizhen Xiang:** Writing – review & editing, Supervision, Methodology, Conceptualization.

Declaration of competing interest

The authors declare that they have no known competing financial interests or personal relationships that could have appeared to influence the work reported in this paper.

Acknowledgments

This work is supported by National Natural Science Foundation of China (Nos. 12272061 and 12372355), and National Key Research and Development Program of China (No. 2024YFA1012101).

Appendix A. Proof of the symmetry and positive definiteness of $\hat{\mathbf{C}}$, $\hat{\mathbf{D}}$, $\hat{\mathbf{F}}$

In this appendix, we demonstrate that the homogenized tensors $\hat{\mathbf{C}}$, $\hat{\mathbf{D}}$, and $\hat{\mathbf{F}}$ —as defined in Eqs. (14a), (14c), and (17c)—are symmetric and positive definite.

The symmetry properties follow directly from the definitions of the effective tensors and the intrinsic symmetries of the local elasticity tensor \mathbf{C} . In particular, the following relations hold:

$$\hat{C}_{ijkl} = \hat{C}_{jikl} = \hat{C}_{klji}, \quad \hat{D}_{ijklmn} = \hat{D}_{jiklmn} = \hat{D}_{lmnijk}, \quad \hat{F}_{ijkl} = \hat{F}_{jikl} = \hat{F}_{klji}. \quad (\text{A.1})$$

To establish the positive definiteness of the effective tensors, we begin by demonstrating the linear independence of the first-order cell functions \mathbf{N}^{pq} , as formalized in the following lemma. For clarity, we define the spaces of symmetric second- and third-order tensors as follows:

$$\text{sym}(\mathbb{R}^{3\times 3}) = \{\mathbf{m} \in \mathbb{R}^{3\times 3} \mid m_{ij} = m_{ji}\}, \quad (\text{A.2})$$

$$\text{sym}(\mathbb{R}^{3\times 3\times 3}) = \{\boldsymbol{\eta} \in \mathbb{R}^{3\times 3\times 3} \mid \eta_{ijk} = \eta_{jik}\}. \quad (\text{A.3})$$

Lemma 1. Let \mathbf{C} be symmetric and positive definite, i.e., there exists a constant $\alpha_0 > 0$ such that for all $\mathbf{m} \in \text{sym}(\mathbb{R}^{3\times 3})$ and $\mathbf{y} \in Y_s = Y \setminus C$,

$$\alpha_0 \|\mathbf{m}\|_F^2 \leq C_{ijkl}(\mathbf{y}) m_{ij} m_{kl}, \quad (\text{A.4})$$

where $\|\cdot\|_F$ denotes the Frobenius norm, defined for a matrix $\mathbf{A} = (a_{ij})$ by

$$\|\mathbf{A}\|_F = \sqrt{\sum_{i,j} a_{ij}^2}, \quad (\text{A.5})$$

and analogously for higher-order tensors. Then, for any nonzero $\mathbf{m} \in \text{sym}(\mathbb{R}^{3\times 3})$, we have

$$\sum_{p,q} m_{pq} \mathbf{N}^{pq} \not\equiv 0 \quad \text{in the sense of } D(Y_s). \quad (\text{A.6})$$

Proof. By multiplying both sides of Eq. (9) by m_{pq} and summing over $\{p, q\}$, we obtain:

$$\begin{cases} \frac{\partial}{\partial y_j} (C_{ijkl} e_{ykl} (m_{pq} \mathbf{N}^{pq}) + m_{pq} C_{ijpq}) = 0, & \text{in } Y_s, \\ (C_{ijkl} e_{ykl} (m_{pq} \mathbf{N}^{pq}) + m_{pq} C_{ijpq}) n_j = 0, & \text{on } C^\pm, \\ m_{pq} \mathbf{N}^{pq} \in D(Y_s). \end{cases} \quad (\text{A.7})$$

The variational form of the above equation reads:

$$\int_{Y_s} C_{ijkl} e_{ykl} (m_{pq} \mathbf{N}^{pq}) e_{ij}(\mathbf{v}) + m_{pq} C_{ijpq} e_{ij}(\mathbf{v}) \, d\mathbf{y} = 0, \quad \forall \mathbf{v} \in D(Y_s). \quad (\text{A.8})$$

Since $\mathbf{m} \neq 0$, the positive definiteness of \mathbf{C} (see Eq. (A.4)) guarantees the existence of indices i_0, j_0 such that

$$m_{pq} C_{i_0 j_0 pq}(\mathbf{y}) \neq 0, \quad \forall \mathbf{y} \in Y_s.$$

Assume, for contradiction, that $m_{pq} \mathbf{N}^{pq} = 0$. Then the variational equation reduces to:

$$\int_{Y_s} m_{pq} C_{ijpq} e_{ij}(\mathbf{v}) \, d\mathbf{y} = 0, \quad \forall \mathbf{v} \in D(Y_s), \quad (\text{A.9})$$

which leads to a contradiction, since a non-zero function (namely $m_{pq} C_{i_0 j_0 pq}$) on a set of positive measure cannot have vanishing integral against all test functions $e_{i_0 j_0}(\mathbf{v})$.

Therefore, $\sum_{p,q} m_{pq} \mathbf{N}^{pq} \not\equiv 0$ in $D(Y_s)$, and the linear independence is established. \square

Notably, the higher-order stiffness tensor $\hat{\mathbf{D}}$ can be decomposed as $\hat{D}_{ijklmn} = \hat{D}_{ijklmn}^1 + \hat{D}_{ijklmn}^2$, where

$$\hat{D}_{ijklmn}^1 = \int_{Y_s} C_{pkqn} \mathbf{N}_p^{ij} \mathbf{N}_q^{lm} \, d\mathbf{y}, \quad (\text{A.10})$$

$$\hat{D}_{ijklmn}^2 = \int_{Y_s} C_{pqrs} e_{ypq} (\mathbf{N}^{ijk}) e_{yrs} (\mathbf{N}^{lmn}) \, d\mathbf{y}. \quad (\text{A.11})$$

Based on our previous work (Li et al., 2025), the linear independence of the first-order cell functions \mathbf{N}^{pq} implies the positive definiteness of the effective tensors $\hat{\mathbf{C}}$, $\hat{\mathbf{D}}^1$, and $\hat{\mathbf{F}}$. Specifically, there exist constants $\alpha_1 > 0$, $\alpha_2 > 0$, and $\alpha_3 > 0$, such that for any symmetric strain tensor $\mathbf{m} \in \text{sym}(\mathbb{R}^{3\times 3})$ and any symmetric strain gradient tensor $\boldsymbol{\eta} \in \text{sym}(\mathbb{R}^{3\times 3\times 3})$, the following inequalities hold:

$$m_{ij} \hat{C}_{ijkl} m_{kl} \geq \alpha_1 \|\mathbf{m}\|_F^2, \quad \eta_{ijk} \hat{D}_{ijklmn}^1 \eta_{lmn} \geq \alpha_2 \|\boldsymbol{\eta}\|_F^2, \quad m_{ij} \hat{F}_{ijkl} m_{kl} \geq \alpha_3 \|\mathbf{m}\|_F^2. \quad (\text{A.12a})$$

$$\begin{pmatrix} \hat{C}_{1111} & \hat{C}_{1122} & \hat{C}_{1133} \\ \hat{C}_{1111} & \hat{C}_{1133} \\ \hat{C}_{3333} \\ & \hat{C}_{1212} \\ & & \hat{C}_{2323} \\ & & & \hat{C}_{1313} \end{pmatrix}$$

Fig. B.24. The Voigt structure of tensor $\hat{\mathbf{C}}$.

$$\begin{pmatrix} \hat{D}_{111111} \hat{D}_{111221} \hat{D}_{111122} \hat{D}_{111331} \hat{D}_{111133} \\ \hat{D}_{221221} \hat{D}_{221122} \hat{D}_{221331} \hat{D}_{221133} \\ \hat{D}_{122122} \hat{D}_{122331} \hat{D}_{122133} \\ \hat{D}_{331331} \hat{D}_{331133} \\ \hat{D}_{133133} \\ \hline \hat{D}_{222222} \hat{D}_{222112} \hat{D}_{222121} \hat{D}_{222332} \hat{D}_{222233} \\ \hat{D}_{112112} \hat{D}_{112121} \hat{D}_{112332} \hat{D}_{112233} \\ \hat{D}_{121121} \hat{D}_{121332} \hat{D}_{121233} \\ \hat{D}_{332332} \hat{D}_{332233} \\ \hat{D}_{233233} \\ \hline \hat{D}_{333333} \hat{D}_{333113} \hat{D}_{333131} \hat{D}_{333223} \hat{D}_{333232} \\ \hat{D}_{113113} \hat{D}_{113131} \hat{D}_{113223} \hat{D}_{113232} \\ \hat{D}_{131131} \hat{D}_{131223} \hat{D}_{131232} \\ \hat{D}_{223223} \hat{D}_{223323} \\ \hat{D}_{232232} \\ \hline \hat{D}_{231231} \hat{D}_{231123} \hat{D}_{231132} \\ \hat{D}_{123123} \hat{D}_{123132} \\ \hat{D}_{132132} \end{pmatrix}$$

Fig. B.25. The Voigt structure of tensor $\hat{\mathbf{D}}$. (For interpretation of the references to color in this figure legend, the reader is referred to the web version of this article.)

According to the definition of $\hat{\mathbf{D}}^2$, we have:

$$\eta_{ijk} \hat{D}_{ijklmn}^2 \eta_{lmn} = \int_{Y_s} C_{pqrs} e_{ypq}(\eta_{ijk} \mathbf{N}^{ijk}) e_{yrs}(\eta_{lmn} \mathbf{N}^{lmn}) dy \geq \alpha_0 \|e_{ypq}(\eta_{ijk} \mathbf{N}^{ijk})\|_F^2 \geq 0. \quad (\text{A.13})$$

Consequently, the total effective higher-order tensor $\hat{\mathbf{D}}$ satisfies:

$$\eta_{ijk} \hat{D}_{ijklmn} \eta_{lmn} = \eta_{ijk} \hat{D}_{ijklmn}^1 \eta_{lmn} + \eta_{ijk} \hat{D}_{ijklmn}^2 \eta_{lmn} \geq \alpha_0 \|\eta\|_F^2, \quad (\text{A.14})$$

which establishes the positive definiteness of $\hat{\mathbf{D}}$.

Appendix B. Independent components of tensors $\hat{\mathbf{C}}, \hat{\mathbf{D}}, \hat{\mathbf{F}}$

From the definitions of $\hat{\mathbf{C}}, \hat{\mathbf{D}}, \hat{\mathbf{F}}$ in Eqs. (14a), (14c), and (17c), the following symmetry properties can be derived:

$$\hat{C}_{ijkl} = \hat{C}_{jikl} = \hat{C}_{klij}, \quad \hat{D}_{pqjmln} = \hat{D}_{qpjmln} = \hat{D}_{mnlpqj}, \quad \hat{F}_{ijkl} = \hat{F}_{jikl} = \hat{F}_{klij}. \quad (\text{B.1})$$

In this work, the material microstructure is modeled by a RVE containing a penny-shaped crack, which induces transverse isotropy characterized by $O(2)$ -invariance. Specifically, the material exhibits continuous rotational symmetry (∞ -invariance) about the e_3 -axis and reflectional symmetry (π -invariance) about any in-plane axis. As a consequence, the homogenized elasticity tensor $\hat{\mathbf{C}}$ possesses five independent components. The corresponding Voigt matrix structure of $\hat{\mathbf{C}}$ is shown in Fig. B.24, where $\hat{C}_{1212} = \frac{1}{2}(\hat{C}_{1111} - \hat{C}_{1122})$.

For the tensor $\hat{\mathbf{D}}$, the number of independent components is 21 due to the transversely isotropic symmetry of the RVE (Auffray et al., 2013). The structure of $\hat{\mathbf{D}}$ is shown in Fig. B.25. In Fig. B.25, four diagonal blocks are visible, and the first two 5×5 blocks are equal. Within each block, unequal components are marked with different colors, except for the black color, which represents a unique component. For example, in the fourth 3×3 block on the diagonal, we observe that $\hat{D}_{231123} = \hat{D}_{123132}$ and $\hat{D}_{231231} = \hat{D}_{132132}$, but \hat{D}_{231132} is independent of \hat{D}_{123123} .

For the tensor $\hat{\mathbf{F}}$, there are four independent components. Its Voigt representation and the distribution of nonzero independent entries closely resemble those of the effective stiffness tensor $\hat{\mathbf{C}}$, with the exception that $\hat{F}_{1111} = \hat{F}_{1122}$, which further implies $\hat{F}_{1212} = \frac{1}{2}(\hat{F}_{1111} - \hat{F}_{1122}) = 0$, as illustrated in Fig. B.26. These identities can be derived from the definition of $\hat{\mathbf{F}}$ and the symmetry properties of the associated first-order cell functions.

Appendix C. Clausius–duhem inequality

In this section, we show that the proposed fracture model complies with the Clausius–Duhem inequality for dissipation. For the quasi-static case, the inequality must hold in the form (including strain-gradient contributions) (Peerlings et al., 2004; Nguyen and Niiranen, 2020)

$$\Sigma_{ij} \dot{\mathcal{E}}_{ij} + \Gamma_{ijk} \dot{\mathcal{E}}_{ijk} - \dot{\Psi} \geq 0. \quad (\text{C.1})$$

$$\begin{pmatrix} \hat{F}_{1111} & \hat{F}_{1111} & \hat{F}_{1133} \\ \hat{F}_{1111} & \hat{F}_{1133} & \\ \hat{F}_{3333} & & \\ & 0 & \\ & & \hat{F}_{2323} \\ & & & \hat{F}_{1313} \end{pmatrix}$$

Fig. B.26. The Voigt structure of tensor $\hat{\mathbf{F}}$.

The internal energy is defined as

$$\Psi = \frac{1}{2} \hat{C}_{ijkl} \mathcal{E}_{ij} \mathcal{E}_{kl} + \frac{\varepsilon^2}{2} \hat{D}_{ijklmn} \mathcal{E}_{ijk} \mathcal{E}_{lmn} + \frac{1}{\varepsilon} G_c S. \quad (\text{C.2})$$

Substituting the constitutive relations in Eq. (24), one obtains

$$\begin{aligned} \Sigma_{ij} \dot{\mathcal{E}}_{ij} + \Gamma_{ijk} \dot{\mathcal{E}}_{ijk} - \dot{\Psi} &= \Sigma_{ij} \dot{\mathcal{E}}_{ij} + \Gamma_{ijk} \dot{\mathcal{E}}_{ijk} - \frac{\partial \Psi}{\partial \mathcal{E}_{ij}} \dot{\mathcal{E}}_{ij} - \frac{\partial \Psi}{\partial \mathcal{E}_{ijk}} \dot{\mathcal{E}}_{ijk} - \frac{\partial \Psi}{\partial S} \dot{S} \\ &= -\frac{\partial \Psi}{\partial S} \dot{S} = -\left(\frac{1}{2} \frac{\partial \hat{C}_{ijkl}}{\partial S} \mathcal{E}_{ij} \mathcal{E}_{kl} + \frac{\varepsilon^2}{2} \frac{\partial \hat{D}_{ijklmn}}{\partial S} \mathcal{E}_{ijk} \mathcal{E}_{lmn} + \frac{1}{\varepsilon} G_c \right) \dot{S} \\ &= \frac{1}{\varepsilon} (G^{\text{static}} - G_c) \dot{S}. \end{aligned} \quad (\text{C.3})$$

According to the static damage law, when $G^{\text{static}} \geq G_c$, one has $\dot{S} > 0$; otherwise, $\dot{S} = 0$. Therefore, the inequality (C.1) is rigorously satisfied.

For dynamic fracture, the strain-rate terms in the homogenized kinetic energy can be regarded as the contribution of micro-inertia to the macroscopic internal energy, i.e.,

$$\Psi = \frac{1}{2} \hat{C}_{ijkl} \mathcal{E}_{ij} \mathcal{E}_{kl} + \frac{\varepsilon^2}{2} \hat{D}_{ijklmn} \mathcal{E}_{ijk} \mathcal{E}_{lmn} + \frac{1}{\varepsilon} \hat{F}_{ijkl} \dot{\mathcal{E}}_{ij} \dot{\mathcal{E}}_{kl} + \frac{1}{\varepsilon} G_c S. \quad (\text{C.4})$$

The corresponding Clausius–Duhem inequality then includes both strain-gradient and strain-rate contributions:

$$\Sigma_{ij} \dot{\mathcal{E}}_{ij} + \Gamma_{ijk} \dot{\mathcal{E}}_{ijk} + \varepsilon^2 \hat{F}_{ijkl} \ddot{\mathcal{E}}_{kl} \dot{\mathcal{E}}_{ij} - \dot{\Psi} \geq 0. \quad (\text{C.5})$$

Using the constitutive relations (24) and the damage/fracture evolution law (32), it can similarly be verified that the dynamic fracture model satisfies this inequality.

Data availability

Data will be made available on request.

References

- Admal, N.C., Marian, J., Po, G., 2017. The atomistic representation of first strain-gradient elastic tensors. *J. Mech. Phys. Solids* 99, 93–115.
- Ahmadi, G., Firoozbakhsh, K., 1975. First strain gradient theory of thermoelasticity. *Int. J. Solids Struct.* 11, 339–345.
- Aifantis, E.C., 1992. On the role of gradients in the localization of deformation and fracture. *Internat. J. Engrg. Sci.* 30, 1279–1299.
- Aifantis, E.C., 1999. Strain gradient interpretation of size effects. *Fract. Scaling* 29, 9–314.
- Aifantis, E.C., 2003. Update on a class of gradient theories. *Mech. Mater.* 35, 259–280.
- Amouzou-Adoun, Y.A., Jebahi, M., Forest, S., Fivel, M., 2024. Advanced modeling of higher-order kinematic hardening in strain gradient crystal plasticity based on discrete dislocation dynamics. *J. Mech. Phys. Solids* 193, 105875.
- Antoun, T., Seaman, L., Curran, D.R., Kanel, G.I., Razorenov, S.V., Utkin, A.V., 2003. Spall Fracture. Springer Science & Business Media..
- Askes, H., Aifantis, E.C., 2011. Gradient elasticity in statics and dynamics: an overview of formulations, length scale identification procedures, finite element implementations and new results. *International. J. Solids Struct.* 48, 1962–1990.
- Auffray, N., Quang, H.L.E., He, Q.C., 2013. Matrix representations for 3d strain-gradient elasticity. *J. Mech. Phys. Solids* 61, 1202–1223. <http://dx.doi.org/10.1016/j.jmps.2013.01.003>, <https://www.sciencedirect.com/science/article/pii/S0022509613000203>.
- Bacigalupo, A., Gambarotta, L., 2012. Computational two-scale homogenization of periodic masonry: characteristic lengths and dispersive waves. *Comput. Methods Appl. Mech. Engrg.* 213, 16–28.
- Bacigalupo, A., Gambarotta, L., 2014. Second-gradient homogenized model for wave propagation in heterogeneous periodic media. *Int. J. Solids Struct.* 51, 1052–1065.
- Bacquaut, G., Bleyer, J., Maurini, C., 2025. Regularization of softening plasticity with the cumulative plastic strain-rate gradient. *J. Mech. Phys. Solids* 194, 105923.
- Bakhvalov, N., Panasenko, G., 1989. Homogenisation: Averaging processes in periodic media. *Math. Appl.*
- Barbours, S., Li, J., 2018. Establishment of strain gradient constitutive relations by using asymptotic analysis and the finite element method for complex periodic microstructures. *Int. J. Solids Struct.* 136, 60–76.
- Bensoussan, A., Lions, J.L., Papanicolaou, G., Caughey, T., 1979. Asymptotic analysis of periodic structures. *J. Appl. Mech.* 46 (477).
- Berezovski, A., Yildizdag, M.E., Scerrato, D., 2020. On the wave dispersion in microstructured solids. *Contin. Mech. Thermodyn.* 32, 569–588.
- Bourdin, B., Larsen, C.J., Richardson, C.L., 2011. A time-discrete model for dynamic fracture based on crack regularization. *Int. J. Fract.* 168, 133–143.
- Boutin, C., 1996. Microstructural effects in elastic composites. *Int. J. Solids Struct.* 33, 1023–1051.
- Brenner, S.C., Neilan, M., 2011. A C^0 interior penalty method for a fourth order elliptic singular perturbation problem. *SIAM J. Numer. Anal.* 49, 869–892.
- Cadoni, E., Labibes, K., Albertini, C., Berra, M., Giangrasso, M., 2001. Strain-rate effect on the tensile behaviour of concrete at different relative humidity levels. *Mater. Struct.* 34, 21–26.
- Cannizzo, A., Giordano, S., 2023. Thermal effects on fracture and the brittle-to-ductile transition. *Phys. Rev. E* 107, 035001.
- Chen, W., Fish, J., 2001. A dispersive model for wave propagation in periodic heterogeneous media based on homogenization with multiple spatial and temporal scales. *J. Appl. Mech.* 68, 153–161.
- Dascalu, C., 2024. A damage law for dynamic failure in brittle solids with penny-shaped microcracks. *J. Dyn. Behav. Mater.* 10, 170–180.

- Dascalu, C., Bilbie, G., Agiasofitou, E., 2008. Damage and size effects in elastic solids: A homogenization approach. *Int. J. Solids Struct.* 45, 409–430.
- Díaz-Rubio, F.G., Perez, J.R., Gálvez, V.S., 2002. The spalling of long bars as a reliable method of measuring the dynamic tensile strength of ceramics. *Int. J. Impact Eng.* 27, 161–177.
- Drugan, W., 2000. Micromechanics-based variational estimates for a higher-order nonlocal constitutive equation and optimal choice of effective moduli for elastic composites. *J. Mech. Phys. Solids* 48, 1359–1387.
- Erzar, B., Forquin, P., 2010. An experimental method to determine the tensile strength of concrete at high rates of strain. *Exp. Mech.* 50, 941–955.
- Erzar, B., Forquin, P., 2011. Experiments and mesoscopic modelling of dynamic testing of concrete. *Mech. Mater.* 43, 505–527.
- Fleck, N., Muller, G., Ashby, M.F., Hutchinson, J.W., 1994. Strain gradient plasticity: theory and experiment. *Acta Met. et Mater.* 42, 475–487.
- Forquin, P., Erzar, B., 2009. Dynamic fragmentation process in concrete under impact and spalling tests. In: IUTAM Symposium on Dynamic Fracture and Fragmentation. Springer, pp. 447–469.
- Freund, L.B., 1990. Dynamic Fracture Mechanics. Cambridge University Press.
- Gabet, T., 2006. Comportement triaxial du béton sous fortes contraintes: Influence du trajet de chargement. (Ph.D. thesis). Université Joseph-Fourier-Grenoble I.
- Gálvez, F., Rodríguez, J., Gálvez, V.S., 2000. Influence of the strain rate on the tensile strength in aluminas of different purity. *Le J. de Phys. IV* 10, Pr9–323.
- Gambarotta, L., Lagomarsino, S., 1993. A microcrack damage model for brittle materials. *Int. J. Solids Struct.* 30, 177–198.
- Geers, M.G., Kouznetsova, V., Brekelmans, W., 2001. Gradient-enhanced computational homogenization for the micro-macro scale transition. *Le J. de Phys. IV* 11, Pr5–145.
- Gitman, I.M., Askes, H., Kuhl, E., Aifantis, E.C., 2009. Stress concentrations in fractured compact bone simulated with a special class of anisotropic gradient elasticity. *Int. J. Solids Struct.* 47, 1099–1107.
- Grassl, P., Grégoire, D., Solano, L.R., Pijaudier-Cabot, G., 2012. Meso-scale modelling of the size effect on the fracture process zone of concrete. *Int. J. Solids Struct.* 49, 1818–1827.
- Griffith, A.A., 1921. Vi. the phenomena of rupture and flow in solids. Philosophical transactions of the royal society of london. In: Series A, containing papers of a mathematical or physical character, vol. 221, pp. 163–198.
- Gross, D., Seelig, T., 2017. Fracture Mechanics: With an Introduction To Micromechanics. Springer.
- Gross, D., Zhang, C., 1992. Wave propagation in damaged solids. *Int. J. Solids Struct.* 29, 1763–1779.
- Gurtin, M.E., 2000. On the plasticity of single crystals: free energy, microforces, plastic-strain gradients. *J. Mech. Phys. Solids* 48, 989–1036.
- Hahn, G.T., 1984. The influence of microstructure on brittle fracture toughness.
- Hall, E., 1951. The deformation and ageing of mild steel: Iii discussion of results. *Proc. Phys. Soc. Sect. B* 64 (747).
- Hosseini, S., Niiranen, J., 2022. 3D strain gradient elasticity: Variational formulations, isogeometric analysis and model peculiarities. *Comput. Methods Appl. Mech. Engrg.* 389, 114324.
- Irwin, G., 1957. Analysis of stresses and strains near the end of a crack traversing a plate. *J. Appl. Mech.* 24, 361–364.
- Irwin, G.R., 1958. Fracture. *Elast. Plasticity/Elastizität Und Plastizität* 55, 1–590.
- Jebahi, M., Forest, S., 2023. An alternative way to describe thermodynamically-consistent higher-order dissipation within strain gradient plasticity. *J. Mech. Phys. Solids* 170, 105103.
- Keita, O., Dascalu, C., François, B., 2014. A two-scale model for dynamic damage evolution. *J. Mech. Phys. Solids* 64, 170–183.
- Kouznetsova, V., Geers, M.G., Brekelmans, W.M., 2002. Multi-scale constitutive modelling of heterogeneous materials with a gradient-enhanced computational homogenization scheme. *Internat. J. Numer. Methods Engrg.* 54, 1235–1260.
- Lam, D.C., Yang, F., Chong, A., Wang, J., Tong, P., 2003. Experiments and theory in strain gradient elasticity. *J. Mech. Phys. Solids* 51, 1477–1508.
- Lazar, M., Po, G., 2015. The non-singular green tensor of mindlin's anisotropic gradient elasticity with separable weak non-locality. *Phys. Lett. A* 379, 1538–1543.
- Li, J., 2011a. A micromechanics-based strain gradient damage model for fracture prediction of brittle materials—part i: Homogenization methodology and constitutive relations. *Int. J. Solids Struct.* 48, 3336–3345.
- Li, J., 2011b. A micromechanics-based strain gradient damage model for fracture prediction of brittle materials—part ii: Homogenization methodology and constitutive relations. *Int. J. Solids Struct.* 48, 3336–3345.
- Li, X., Li, H., Zhang, Q., Jiang, J., Zhao, J., 2018. Dynamic fragmentation of rock material: characteristic size, fragment distribution and pulverization law. *Eng. Fract. Mech.* 199, 739–759.
- Li, J., Pham, T., Abdelmoula, R., Song, F., Jiang, C., 2011a. A micromechanics-based strain gradient damage model for fracture prediction of brittle materials—part ii: Damage modeling and numerical simulations. *Int. J. Solids Struct.* 48, 3346–3358.
- Li, J., Pham, T., Abdelmoula, R., Song, F., Jiang, C., 2011b. A micromechanics-based strain gradient damage model for fracture prediction of brittle materials—part ii: Damage modeling and numerical simulations. *Int. J. Solids Struct.* 48, 3346–3358.
- Li, Q., Rao, Y., Yang, Z., Cui, J., Xiang, M., 2025. Asymptotic homogenization-based strain gradient elastodynamics: Governing equations, well-posedness and numerical examples. *Comput. Methods Appl. Mech. Engrg.* 442, 118010.
- Liebold, C., Müller, W., 2015. Applications of strain gradient theories to the size effect in submicro-structures incl. experimental analysis of elastic material parameters. *Bull. TICMI* 19, 45–55.
- Makvandi, R., Duczek, S., Juhre, D., 2019. A phase-field fracture model based on strain gradient elasticity. *Eng. Fract. Mech.* 220, 106648.
- Maranganti, R., Sharma, P., 2007. A novel atomistic approach to determine strain-gradient elasticity constants: Tabulation and comparison for various metals, semiconductors, silica, polymers and the (ir) relevance for nanotechnologies. *J. Mech. Phys. Solids* 55, 1823–1852.
- Martínez-Pañeda, E., Niordson, C.F., 2016. On fracture in finite strain gradient plasticity. *Int. J. Plast.* 80, 154–167.
- Mier, J.Van., Vliet, M.Van., 2003. Influence of microstructure of concrete on size/scale effects in tensile fracture. *Eng. Fract. Mech.* 70, 2281–2306.
- Mindlin, R.D., 1965. Second gradient of strain and surface-tension in linear elasticity. *Int. J. Solids Struct.* 1, 417–438.
- Mindlin, R.D., Eshel, N., 1968. On first strain-gradient theories in linear elasticity. *Int. J. Solids Struct.* 4, 109–124.
- Nguyen, T.H., Niiranen, J., 2020. A second strain gradient damage model with a numerical implementation for quasi-brittle materials with micro-architectures. *Math. Mech. Solids* 25, 515–546.
- Niiranen, J., Khakalo, S., Balobanov, V., Niemi, A.H., 2016. Variational formulation and isogeometric analysis for fourth-order boundary value problems of gradient-elastic bar and plane strain/stress problems. *Comput. Methods Appl. Mech. Engrg.* 308, 182–211.
- Nix, W.D., Gao, H., 1998. Indentation size effects in crystalline materials: a law for strain gradient plasticity. *J. Mech. Phys. Solids* 46, 411–425.
- Oleinik, O., Shamaev, A., Yosifian, G., 1992. Mathematical Problems in Elasticity and Homogenization. Elsevier.
- Peerlings, R., Fleck, N., 2004. Computational evaluation of strain gradient elasticity constants. *Int. J. Multiscale Comput. Eng.* 2.
- Peerlings, R., Massart, T., Geers, M., 2004. A thermodynamically motivated implicit gradient damage framework and its application to brick masonry cracking. *Comput. Methods Appl. Mech. Engrg.* 193, 3403–3417.
- Petch, N.J., 1953. The cleavage strength of polycrystals. *J. Iron Steel Inst.* 174, 25–28.
- Placidi, L., Barchiesi, E., 2019. Energy approach to brittle fracture in strain-gradient modelling. *Proceedings of the royal society a: Mathematical. Phys. Eng. Sci.* 474, 20170878.
- Placidi, L., Barchiesi, E., Misra, A., 2018a. A strain gradient variational approach to damage: a comparison with damage gradient models and numerical results. *Math. Mech. Complex Syst.* 6, 77–100.
- Placidi, L., Misra, A., Barchiesi, E., 2018b. Two-dimensional strain gradient damage modeling: a variational approach. *Z. Für Angewandte Math. Und Phys.* 69, 1–19.
- Placidi, L., Misra, A., Barchiesi, E., 2019. Simulation results for damage with evolving microstructure and growing strain gradient moduli. *Contin. Mech. Thermodyn.* 31, 1143–1163.
- Poncelet, M., Somera, A., Morel, C., Jalin, C., Auffray, N., 2018. An experimental evidence of the failure of cauchy elasticity for the overall modeling of a non-centro-symmetric lattice under static loading. *Int. J. Solids Struct.* 147, 223–237.
- Rafiee, S., Gross, D., Seelig, T., 2004. The influence of microcrack nucleation on dynamic crack growth—a numerical study. *Eng. Fract. Mech.* 71, 849–857.
- Rao, Y., Xiang, M., Cui, J., 2022. A strain gradient brittle fracture model based on two-scale asymptotic analysis. *J. Mech. Phys. Solids* 104752.
- Rao, Y., Xiang, M., Li, Q., Cui, J., 2023. A unified two-scale theory for modeling microstructural length scale. *Strain Gradient Strain Rate Eff. Brittle Fract.* *Int. J. Solids Struct.* 112176.
- Ravi-Chandar, K., Yang, B., 1997. On the role of microcracks in the dynamic fracture of brittle materials. *J. Mech. Phys. Solids* 45, 535–563.
- Rice, J., 1978. Thermodynamics of the quasi-static growth of griffith cracks. *J. Mech. Phys. Solids* 26, 61–78.
- Rosi, G., Auffray, N., 2016. Anisotropic and dispersive wave propagation within strain-gradient framework. *Wave Motion* 63, 120–134.

- Shishesaz, M., Hosseini, M., Tahan, K.Naderan., Hadi, A., 2017. Analysis of functionally graded nanodisks under thermoelastic loading based on the strain gradient theory. *Acta Mech.* 228, 4141–4168.
- Smyshlyaev, V.P., Cherednichenko, K.D., 2000. On rigorous derivation of strain gradient effects in the overall behaviour of periodic heterogeneous media. *J. Mech. Phys. Solids* 48, 1325–1357.
- Sunyk, R., Steinmann, P., 2003. On higher gradients in continuum-atomistic modelling. *Int. J. Solids Struct.* 40, 6877–6896.
- Terada, K., Kikuchi, N., 2001. A class of general algorithms for multi-scale analyses of heterogeneous media. *Comput. Methods Appl. Mech. Engrg.* 190, 5427–5464.
- Toupin, R., 1962. Elastic materials with couple-stresses. *Arch. Ration. Mech. Anal.* 11, 385–414.
- Toutlemonde, F., 1994. Résistance au choc des structures en béton: du comportement du matériau au calcul des ouvrages. Ecole Nationale des Ponts et Chaussées. (Ph.D. thesis).
- Triantafyllidis, N., Bardenhagen, S., 1996. The influence of scale size on the stability of periodic solids and the role of associated higher order gradient continuum models. *J. Mech. Phys. Solids* 44, 1891–1928.
- Xiang, M., Cui, J., Li, B., Tian, X., 2012. Atom-continuum coupled model for thermo-mechanical behavior of materials in micro-nano scales. *Sci. China Phys. Mech. Astron.* 55, 1125–1137.
- Yang, H., Abali, B.E., Müller, W.H., Barboura, S., Li, J., 2022. Verification of asymptotic homogenization method developed for periodic architected materials in strain gradient continuum. *Int. J. Solids Struct.* 238, 111386.
- Yang, H., Abali, B.E., Timofeev, D., Müller, W.H., 2020. Determination of metamaterial parameters by means of a homogenization approach based on asymptotic analysis. *Contin. Mech. Thermodyn.* 32, 1251–1270.
- Yang, H., Liu, Z., Xia, Y., Fan, W., Taylor, A.C., Han, X., 2024. Mechanical properties of hierarchical lattice via strain gradient homogenization approach. *Compos. Part B: Eng.* 271, 111153.
- Yang, Z., Rao, Y., Sun, Y., Cui, J., Xiang, M., 2023. A second-order strain gradient fracture model for the brittle materials with micro-cracks by a multiscale asymptotic homogenization. *Comput. Mech.* 1–26.
- Yin, H., Qi, H.J., Fan, F., Zhu, T., Wang, B., Wei, Y., 2015. Griffith criterion for brittle fracture in graphene. *Nano Lett.* 15, 1918–1924.
- You, H., Xiang, M., Jing, Y., Guo, L., Yang, Z., 2025. A strain gradient phase field model for heterogeneous materials based on two-scale asymptotic homogenization. *J. Mech. Phys. Solids* 200, 106104.
- Yvonnet, J., Auffray, N., Monchiet, V., 2020. Computational second-order homogenization of materials with effective anisotropic strain-gradient behavior. *Int. J. Solids Struct.* 191, 434–448.
- Zhou, F., Molinari, J.F., Ramesh, K., 2006. Effects of material properties on the fragmentation of brittle materials. *Int. J. Fract.* 139, 169–196.
- Zinszner, J., Erzar, B., Forquin, P., Buzaud, E., 2015. Dynamic fragmentation of an alumina ceramic subjected to shockless spalling: an experimental and numerical study. *J. Mech. Phys. Solids* 85, 112–127.
- Z.P., Bažant, Planas, J., 2019. Fracture and Size Effect in Concrete and Other Quasibrittle Materials. Routledge.